SvedbergOpen
DISSEMINATIONOFKNOWLEDGE

International Journal of Artificial Intelligence and Machine Learning

Publisher's Home Page: https://www.svedbergopen.com/

Research Paper Open Access

Boundary Condensation of a Two-layer Dirichlet-to-Neumann Air-Gap Operator onto a Reluctance Network: Trace Conformity and Validation on a Surface-Magnet Synchronous Machine

Idris Laouar[1*], Ahcene Boukadoum[1], Nabil Mezhoud[1], Salima Lekhchine[2]

[1]Department of Electrical Engineering, Electrotechnical Laboratory of Skikda (LES), University 20 August 1955 Skikda, 26 Road El Hadaiek, 21000 Skikda, Algeria.
[2]Department of Electrical Engineering, LGMM Laboratory, University 20 August 1955 Skikda, 26 Road El Hadaiek, 21000 Skikda, Algeria.
*Corresponding author(s). E-mail(s): idris.laouar@univ-skikda.dz (ORCID 0009-0004-6663-082X); Contributing authors: boukadoum2003@yahoo.fr (ORCID 0000-0001-9238-8249); n.mezhoud@univ-skikda.dz (ORCID 0000-0002-9383-2097); s.lekhchine@univ-skikda.dz (ORCID 0000-0002-4509-5838).

Received: 10 June 2026 Accepted: 23 August 2026 Published: 18 September 2026

Abstract
A reluctance network discretises the iron of an electrical machine but imports its air-gap coupling from a closure whose parameters the geometry does not fix. This paper closes the gap with the exact Dirichlet-to-Neumann operator of the two-layer annulus formed by the air gap and the surface magnets, the magnetisation entering as a source of the same surface map, and condenses it onto the bore nodes of a nonlinear reluctance network solved by Newton on the differential reluctance. The operator is of order one, so its condensation is defined only on a trial space contained in $H^{1/2}$; one potential per node imposes a piecewise-constant bore datum, which lies outside that space. It is proved in closed form that the condensed self-energy of a column grows as $(2\mu_0 L/\pi)\ln N$ with the harmonic truncation N, the divergent part being $(\mu_0 L/\pi)\ln N$ times the sum of the squared jumps of the bore potential; that locking the truncation to the tiling makes the operator converge to a definite limit which is not the continuous one; and that a continuous piecewise-linear basis, still with one unknown per node, restores an absolutely convergent series with a $1/N^2$ tail and a proved error estimate. Direct summation reproduces the closed forms to between 3×10^{-7} and 1.4×10^{-6} at $N = 10^7$ with no fitted constant. On a 750 W, 15-slot/14-pole machine the condensed model, with no fitted air-gap constant, deviates from two-dimensional finite elements by 0.10 % on synchronous inductance, 0.24 % on flux linkage and 0.31 % on the fundamental air-gap flux density, each below the dispersion the tiling alone produces and hence reported as a bound, while the slot sidebands and the cogging torque, governed by the tooth-tip corner singularity, are bracketed. Rotor-position invariance makes a 721-position sweep cost one factorisation, and a five-test procedure audits the finite-element reference without re-solving it.

Keywords: Magnetic equivalent circuit, Reluctance network, Dirichlet-to-Neumann operator, Air-gap modelling, Permanent-magnet synchronous machine, Trace conformity, Finite-element validation.

I. Introduction

A magnetic equivalent circuit (MEC), or reluctance network, discretises the iron of a machine rather than its field [1]–[3]. Each branch is taken from the geometry and from a measured $B(H)$ curve, so saturation enters without approximation and an arbitrary slot profile costs nothing, while the nodal system stays small enough to be swept over rotor positions, currents and speeds; both machine families have been built this way [4]–[7] and the construction is still being extended [8]–[11]. The discretisation stops at the bore. No iron lies between the two surfaces, so there is no path along which to lay a flux tube, and the tooth-to-tooth permeance that stands in for the annulus has to be imported. It is the only quantity in the network not derived from the geometry, and on a surface-mounted machine it does more than close the circuit: the region is two media, and it carries the source.

Two consequences follow for the electrical engineer. A network of radial branches produces no tangential flux density, so the Maxwell stress cannot be formed from the network and the torque follows from a derivative of co-energy, whose harmonic content is then whatever the closure admits; closing the gap of the 750 W machine studied here (Fig. 1a) with Carter's factor suppresses the first slot sideband entirely and leaves the tangential field low by 19.7 % (Table 1, Sect. VII.a). And the consequence does not stay proportional at drive level: the machine is fed from a 500 V dc bus and, near the upper end of its speed range, the terminal envelope of the reference stands at 468 V (Sect. VI.c), so a relative error on the electromotive force reappears on the current magnified by the ratio of the bus voltage to that margin. An air-gap description good to a few percent on flux density is not, on that account, adequate for the drive-level use for which the circuit was adopted.

Four treatments are current, and each carries a limitation that belongs to its construction. An equivalent uniform gap restores the mean flux and discards the rest [12], [13]. A permeance modulation superimposed on the smooth-gap solution restores the slot harmonics [14], and in the complex form of Žarko, Ban and Lipo it returns both field components exactly for a slotted stator facing a smooth rotor [15], [16]; but the modulation is derived in a linear medium, so saturation is assumed away in the one region the network cannot represent. Parametric tooth-to-tooth functions keep the network and the saturable iron together by giving two facing elements a closed-form coupling in their relative misalignment [17], but the decay law is written in the arcs of the elements, so the permeance is a function of the discretisation: implemented as its authors specify, that family is as close to the reference as the operator on the first slot sideband (Sect. VII.a), but over three tangential discretisations of the same machine it changes sign and magnitude on that quantity, over a spread of 219 % (Table 1), and sharpening the coupling cells does not touch that dependence [18]. Solving Laplace's or Poisson's equation analytically in each region [19], [20], generalised by Gysen *et al.* [21], mapping the slotted bore conformally onto a slotless one [22], or matching an analytical annulus to an analytically treated slot or magnet region [23], [24], captures the slot harmonics exactly and fits nothing; but there the iron is infinitely permeable and the regions must remain separable, a recent hybrid model being labelled linear by its own authors [25].

A fifth line needs separate treatment, because the present formulation belongs to it and the mathematical object is not new. Coupling a Fourier expansion of the annulus to a discretised iron domain is the principle of the air-gap element [26], [27], textbook material since Salon [28] and refined into the harmonic sliding-interface conditions of finite-element practice [29], [30], whose mortar and harmonic variants have a stability theory of their own [31]–[33]; such an annulus has been placed beside a reluctance network [34] and remains under development [35]. Condensing it onto its own boundary is the Schur complement of the region, the discretisation of a Steklov–Poincaré operator [36], and the exact operator of a circular boundary is a Fourier multiplier known in closed form [37], [38]: the annulus contributes a dense surface block and no interior unknowns, an established reduction [38] routinely condensed onto trial spaces that are not those of a boundary-element method [39], [40]. Those constructions are the nearest neighbours of the present work, and the conformity question is the one they leave open: in each the trial space is chosen by the interior discretisation, but in each that space is at least continuous, so its trace lies in the energy space and the condensation is conforming without anyone having to say so. A reluctance network in nodal form is the case in which it is not [41]: a node carries one potential, so the trial function on the bore is piecewise constant, and a piecewise-constant function does not lie in $H^{1/2}(\Gamma)$, the trace space on which the map is bounded [42]–[45]. Non-conforming Galerkin methods for the hypersingular operator, of the same order, converge when a mortar, Nitsche or interior-penalty term supplies the missing consistency [46]–[48]; the condensation carries no such term, and refinement cannot repair what is not a matter of resolution. Divergence and slow convergence are moreover hard to separate from outside, since a quantity that moves by a constant amount at every doubling is also what slow convergence looks like. The analysis that separates them is standard [36], [42]–[44]; what is new is the check applied to the trial space a reluctance network imposes, and the fact that it fails.

Three features separate the present construction from the air-gap element as that family is normally built: the condensed region spans two media rather than one, so a surface-magnet rotor requires no matching at the magnet boundary; the magnetisation enters as an inhomogeneous term of the same surface map rather than as a separate source problem; and the trial space on the bore is imposed by the network rather than inherited from a finite-element interpolation. The first two are matters of construction, Table 1 measures what they are worth here, and neither is claimed as a novelty; the third is the subject of this paper. Three recent constructions place the closure inside a reluctance network: radial permeance branches between stator-tooth and rotor-tooth nodes on a 1240 MW turbogenerator, re-formed at each rotor position [8]; an annulus filled with a cell network of 1680 nodes coupled to the stator boundary by overlap permeances [18]; and a reluctance mesh in the same role for a switched-reluctance machine [9]. The first two carry one potential per surface node, so the bore datum is piecewise constant, and the question is posed as one of mesh density; Ghods *et al.* come closest without posing it, a coupling permeance that jumps producing spikes in the computed flux linkage, with smoothing or refinement offered as the remedy. A magnet layer changes where the difficulty bites rather than removing it: where the harmonic tail installs itself is set by U_a, the logarithmic thickness of the air layer alone, and here $U_a = 0.02926$ places it near order 34, against order 330 for a bare gap of logarithmic thickness 3×10^{-3}, so the thick two-layer annulus of a surface-magnet rotor is the exposed case. A second gap is methodological. A reduced-order model is almost always validated against finite elements whose uncertainty is rarely quantified, and the re-entrant tooth-tip corner carries an $r^{\lambda-1}$ singularity with $\lambda < 1$ [49], [50], which leaves corner-governed quantities such as the cogging torque [51] mesh-dependent in the reference as much as in the network: on this machine the magnetostatic cogging reference peaks at order 42, which the least common multiple of 15 and 14 forbids, and two meshing strategies of the same model differ there by a factor of 87. A validation that took the reference at face value would have rejected a correct model.

The question this paper answers is therefore the following: under which condition on the bore trial space does the condensation of an exact air-gap operator onto a reluctance network have a limit as the harmonic truncation grows, and what does the answer cost or gain on a machine? The paper derives the exact two-layer operator, establishes that condition, and couples the operator to a nonlinear mesh solved by Newton on the differential reluctance. The central claim is the condition rather than the operator. Six contributions are stated so that each can be checked or refuted.

1. *Divergence in closed form* (Proposition 1, Corollary 1, Sect. III.a): the condensed self-energy of a column grows as $(2\mu_0 L/\pi)\ln N$, each nearest neighbour falls as $-(\mu_0 L/\pi)\ln N$, entries at two or more columns' distance converge, and on any contiguous tiling the divergent part is $(\mu_0 L/\pi)\ln N$ times the periodic second-difference matrix, whose circulant spectrum fixes the rank and the null space at every truncation.
2. *The conforming repair and its estimate* (Sect. III.b–c, Propositions 2 and 2′): a continuous piecewise-linear basis, still one unknown per node, gives a tail bounded by $3\mu_0 L/(\pi d^2 N^2)$ and a conforming Galerkin method with a proved $Ch^{s-1/2}|u|_{H^s(\Gamma)}$ estimate that survives the locking of the truncation to the tiling, the consistency term of the truncated form being the exact spectral fraction (35).
3. *What the locked chain selects* (Proposition 3, Sect. III.e): under $N = \lfloor M_s/2 \rfloor$ the piecewise-constant operator converges, as the tiling is refined, to a definite circulant operator built from second differences of $\sigma(k) = \mathrm{Ci}(k\pi) - \ln(k\pi)$, neither the continuous operator nor the closed forms, which fixes the saturating deviations −4.28 % and +16.5 %; a diagnostic needing neither (Sect. III.d) separates the regimes from successive increments alone.
4. *The theory reproduced by computation* (Sect. VI.a–b): direct summation reproduces the closed forms to between 3×10^{-7} and 1.4×10^{-6} at $N = 10^7$ with no fitted constant, and released from the tiling the fundamental gap flux density drifts by 0.703 % over eleven doublings in the piecewise-constant basis against 0.023 % in the hat basis.
5. *Physical validation and its floors* (Sect. VI.c): the meshed network, carrying no fitted constant, deviates from two-dimensional finite elements by 0.10 % on synchronous inductance, 0.24 % on flux linkage and 0.31 % on the fundamental gap flux density, and the lumped counterpart, carrying three fitted constants, by 1.24 %, 1.11 % and 0.28 %; each lies below the dispersion the tiling alone produces and is reported as a bound, while the corner-governed sideband and cogging torque are brackets that do not close under refinement.
6. *Consequences and an instrument for the reference* (Sects. VI.c–d, VII): one condensation replaces two coupled regions; position invariance makes a 721-position sweep cost one factorisation; the three fitted air-gap constants disappear rather than being re-identified; and a five-test procedure audits a finite-element reference without re-solving it, which here changed the reading of the cogging torque against the model.

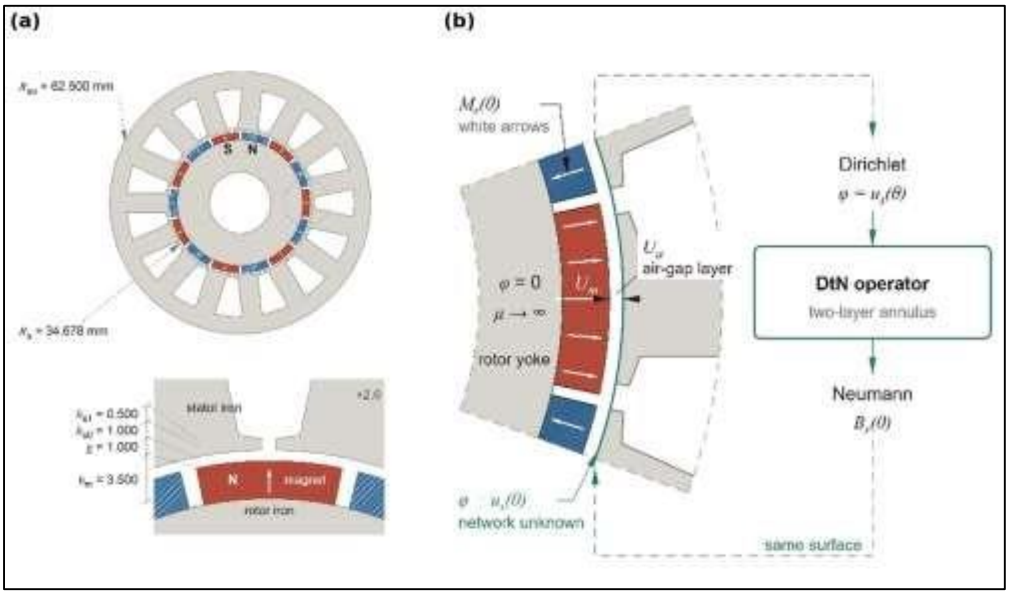

Fig. 1. (a) Cross-section of the 750 W, 15-slot/14-pole surface-mounted PMSM validated in this paper, with its fourteen-sector magnet ring and 2 mm slot openings.

the inset magnifies one slot and its air gap. (b) Geometry of the two-layer annulus condensed by the operator: the magnet layer $r_{mi} \le r \le R_{ro}$ carries the radial magnetisation $M_r(\theta)$ and recoil permeability μ_r, the region $R_{ro} \le r \le R_s$ is air, the rotor back-iron imposes $\varphi(r_{mi}, \theta) = 0$, and the bore potential $u_s(\theta)$ is an unknown carried by the stator reluctance network. The logarithmic thicknesses U_a and U_m of (1) are the natural coordinates of the two layers; the block on the right states the map Sect. II constructs, a Dirichlet datum on the bore returning a Neumann datum on the same surface. The annulus is logarithmically thick, $U_a = 0.02926$ for the air layer alone; the air gap is drawn exaggerated.

Table 1. Air-gap closure at fixed iron model. All network rows (N1–N4) use the same lumped iron network and linear solver at $\mu_r = 3000$, so any difference between them is attributable to the closure alone; tooth-face arc $a_t = 0.361206$ rad, that is 17.40 elements per revolution.

Closure	γ_m	γ_z	elem./rev	$\nu = 8$	$\nu = 22$	B_t rms
N1 smooth + Carter	—	—	—	−100 %	−100 %	−19.7 %
N2 generic cos²	—	—	—	+307.1 %	+144.3 %	−19.7 %
N2b Silva, $a_r = 0.25\, a_t$	0.135452	0.225754	69.58	**−8.7 %**	−45.2 %	−19.7 %
N2b Silva, $a_r = 0.50\, a_t$	0.090301	0.270904	34.79	+170.1 %	+62.1 %	−19.7 %
N2b Silva, $a_r = 1.00\, a_t$	0.000000	0.361206	17.40	−96.4 %	−97.8 %	−19.7 %
N3 operator (this work)	—	—	—	**−8.1 %**	**+7.6 %**	**+7.4 %**
N4 air-gap element	—	—	—	**−13.5 %**	−18.3 %	**+30.4 %**
A1 relative permeance	—	—	—	**−85.0 %**	−91.0 %	**−20.1 %**
A2 complex permeance	—	—	—	**+0.1 %**	−51.0 %	**−10.5 %**
FEA reference				0.01966 T	0.03276 T	0.1333 T

Rows A1 and A2 are complete analytical field models, not closures on that network, evaluated at mid-gap from published implementations of [14] and [15] with no fitted quantity, the slot opening fixing the tooth ratio at 0.86232; their fundamentals are 1.0959 T (+2.0 %) and 1.0876 T (+1.2 %). Every closure of the N1–N2b family returns $B_{g1} = 1.0958$ T (+2.0 %), against 1.0775 T (+0.3 %) for N3, because the mean of each modulation is unity to six decimals; N4 is the same surface operator over a single layer with the magnet meshed, fundamental 1.1210 T (+4.3 %). Orders 8 and 22 are the lower and upper members of the first slot-harmonic pair, $N_s \mp p$. Under the locked chain the tiling alone moves the $\nu = 8$ column by 26.126 % in the piecewise-constant basis and 28.514 % in the hat basis (Table 4), so that column is read as a bound and differences smaller than that band do not order the rows; the spread of 219 % across the three N2b rows, which differ only in the tangential discretisation that sets γ_m and γ_z, does. The transcripts behind rows N4, A1 and A2 are deposited with the rest of the chain.

II. THE TWO-LAYER DIRICHLET-TO-NEUMANN AIR-GAP OPERATOR

a. Hypotheses and boundary-value problem

The annulus between the stator bore R_s and the magnet inner radius r_{mi} (Fig. 1b) is treated under five hypotheses, on which the closed forms of this section and the conformity result of Sect. III rest; where a hypothesis is only approximately met on the test machine, the size of the departure is stated.

H1 (two-dimensional magnetostatics). The field is planar and quasi-static; the annulus carries no current, so the magnetic field derives from a scalar potential, $\mathbf{H} = -\nabla\varphi$, in each of its two media.

H2 (two concentric linear layers). The region is the air layer $R_{ro} \le r \le R_s$ and the magnet layer $r_{mi} \le r \le R_{ro}$, both linear: air of permeability μ_0, and the magnet on its recoil line, $\mathbf{B} = \mu_0\mu_r\mathbf{H} + \mu_0\mathbf{M}$ with a constant recoil permeability μ_r. The inter-magnet gaps are treated as part of the magnet layer with zero magnetisation, which is exact for $\mu_r = 1$ and departs from it by the difference $\mu_r - 1 = 0.039$ on this machine.

H3 (radial magnetisation of a $2p$-pole ring). $\mathbf{M} = M_r(\theta)\hat{\mathbf{r}}$ is independent of r and piecewise constant in θ over each pole of arc ratio α_p, so that it carries only the odd multiples of p [52], [53]. Parallel magnetisation, inter-pole leakage inside the magnet and the radial dependence of the true magnetisation are outside this hypothesis.

H4 (rotor back-iron of infinite permeability). The inner surface of the magnet layer is an equipotential, $\varphi(r_{mi}, \theta) = 0$. This hypothesis is bounded rather than asserted: with $U_m = 0.1097$ the factor $\coth(nU_m)$, through which the rotor boundary reaches the bore, falls to 1.25 at $n = 10$ and 1.03 at $n = 20$, so beyond the lowest orders the magnet layer decouples the rotor iron from the surface and H4 ceases to influence the bore admittance g_n of (9).

H5 (bore datum supplied by the network). The potential on the bore $r = R_s$ is the datum the network supplies; nothing is assumed about the stator iron, which is the network's business.

Writing $v = \ln(r/r_0)$ for a layer of inner radius r_0 turns each layer into a strip of logarithmic thickness

$$U_a = \ln\left(\frac{R_s}{R_{ro}}\right), \qquad U_m = \ln\left(\frac{R_{ro}}{r_{mi}}\right) \tag{1}$$

in which the harmonic solutions are exponentials. In the air layer, with $v = \ln(r/R_{ro})$ and $\varphi_{i,n} = \varphi_n(R_{ro})$ the interface potential,

$$\varphi_n^a(v) = \frac{\varphi_{i,n}\sinh(n(U_a - v)) + u_{s,n}\sinh(nv)}{\sinh(nU_a)} \tag{2}$$

In the magnet layer, $\nabla \cdot \mathbf{B} = 0$ with H2 gives $\mu_r\nabla^2\varphi = \nabla \cdot \mathbf{M}$, and the radial magnetisation of H3 has $\nabla \cdot \mathbf{M} = M_r(\theta)/r$, so the harmonic of order n admits the particular solution

$$\varphi_{p,n}(r) = P_n r, \qquad P_n = \begin{cases} \dfrac{M_n}{\mu_r(1-n^2)}, & n \neq 1 \\ 0, & n = 1 \end{cases} \tag{3}$$

the case $n = 1$ arising only for a two-pole machine, for which the particular solution is of the form $r\ln r$ and is not needed here: with $p = 7$ the magnetisation carries no first-order term, so the value assigned at $n = 1$ in (3) is exact rather than conventional. The complete layer solution adds the homogeneous part; writing $w = \ln(r/r_{mi})$ for the magnet coordinate,

$$\varphi_n^m(w) = C_n\cosh(nw) + A_n\sinh(nw) + P_n r \tag{4}$$

in which the rotor-iron condition, imposed at $w = 0$, gives $C_n = -P_n r_{mi}$, and matching $\varphi_{i,n}$ at R_{ro} gives $A_n = [\varphi_{i,n} - P_n R_{ro} - C_n\cosh(nU_m)]/\sinh(nU_m)$. The lettering matters: C_n multiplies the hyperbolic cosine and A_n the hyperbolic sine, and exchanging them changes the radial structure of the magnet field, and with it the leakage factor and the magnet-loss integral of Sect. VI.c. The magnetisation of a $2p$-pole ring with pole-arc ratio α_p enters through its spectrum, in the classical form given by Zhu and Howe [52], [53],

$$M_n = \begin{cases} \dfrac{4B_{rem}}{\mu_0 m\pi}\sin\dfrac{m\pi\alpha_p}{2}, & n = mp,\ m \text{ odd} \\ 0, & \text{otherwise} \end{cases} \tag{5}$$

which is the only place where the source appears.

b. Response coefficients and bore admittance

Continuity of the potential and of the normal flux density at $r = R_{ro}$,

$$-\mu_0\frac{\partial\varphi^a}{\partial r}\Big|_{R_{ro}} = -\mu_0\mu_r\frac{\partial\varphi^m}{\partial r}\Big|_{R_{ro}} + \mu_0 M_r \tag{6}$$

closes the two-layer system and yields the interface potential $\varphi_{i,n} = \alpha_n u_{s,n} + \beta_n$, so that each harmonic of the bore datum is transferred to the rotor side by α_n and each harmonic of the magnetisation is delivered to the bore by β_n:

$$\alpha_n = \frac{1}{D_n} = [\cosh(nU_a) + \mu_r\sinh(nU_a)\coth(nU_m)]^{-1} \tag{7}$$

$$\beta_n = \frac{R_{ro}\sinh(nU_a)}{nD_n}\left[\mu_r\frac{nP_n}{R_{ro}}\left(R_{ro}\coth(nU_m) - \frac{r_{mi}}{\sinh(nU_m)}\right) - \mu_r P_n + M_n\right] \tag{8}$$

Here $D_n = \cosh(nU_a) + \mu_r\sinh(nU_a)\coth(nU_m)$ is the determinant of the two-layer system; both coefficients follow from (2), (4) and (6) by elimination of A_n and C_n, and β_n has the dimension of a potential (A). The radial flux density at the bore then follows as a linear form in the bore harmonics plus a source term, $B_{r,n}(R_s) = g_n u_{s,n} + b_n$, with

$$g_n = -\mu_0\frac{n}{R_s}\frac{\cosh(nU_a) - \alpha_n}{\sinh(nU_a)} \equiv -\mu_0\frac{n}{R_s}\kappa_n, \qquad b_n = \mu_0\frac{n}{R_s}\frac{\beta_n}{\sinh(nU_a)} \tag{9}$$

This is the Dirichlet-to-Neumann map of the two-layer annulus, g_n in H/m² and b_n in T, and it is the symbol of the corresponding Steklov–Poincaré operator [36]. It spans air and magnet in a single surface relation, so the magnet region requires no matching of its own, and the reduced admittance $\kappa_n = (\cosh(nU_a) - \alpha_n)/\sinh(nU_a)$ isolates what the two-layer structure adds to the bare-gap symbol $-\mu_0 n/R_s$.

c. Projection onto the network surface nodes

A reluctance network in nodal form carries one potential per node [41]. The stator network carries M_s surface nodes, node k spanning an arc of width d_k centred on θ_k at R_s and carrying a uniform potential U_k. Projecting a piecewise-constant potential onto the Fourier basis gives the rectangular operators

$$W^c_{nk} = \frac{2}{n\pi}\sin\left(\frac{nd_k}{2}\right)\cos(n\theta_k), \qquad W^s_{nk} = \frac{2}{n\pi}\sin\left(\frac{nd_k}{2}\right)\sin(n\theta_k) \tag{10}$$

Throughout, a bore quantity $f(\theta)$ is expanded as $\sum_{n\geq 1}(f_n^c\cos n\theta + f_n^s\sin n\theta)$ with real coefficients, and that convention fixes the factors in (10), in (12) and in the torque sum (17). The flux entering the iron through the surface nodes then reads $\mathbf{\Phi}_s = \mathbf{Y}\mathbf{U}_s + \mathbf{i}_{src}(\theta_r)$, in which, with L the active length,

$$\mathbf{Y} = \pi L R_s[(\mathbf{W}^c)^\mathsf{T}\mathrm{diag}(\mathbf{g})\mathbf{W}^c + (\mathbf{W}^s)^\mathsf{T}\mathrm{diag}(\mathbf{g})\mathbf{W}^s] \tag{11}$$

$$\mathbf{i}_{src}(\theta_r) = \pi L R_s[(\mathbf{W}^c)^\mathsf{T}(\mathbf{b}\odot\cos(\mathbf{n}\theta_r)) + (\mathbf{W}^s)^\mathsf{T}(\mathbf{b}\odot\sin(\mathbf{n}\theta_r))] \tag{12}$$

where θ_r is the rotor position and $\odot$ the elementwise product. The flux through column k is $LR_s\int_{\text{arc}\,k}B_r\,d\theta$, and the integral of $\cos n\theta$ over the arc is πW^c_{nk}, which is where the factor $\pi L R_s$ comes from; $\mathbf{Y}$ is in henry and $\mathbf{i}_{src}$ in weber. The condensed block (11) and the source (12) enter the nodal system exactly as any other branch would.

d. Algebraic properties

The matrix of (11) is symmetric by construction and negative semi-definite, since $g_n < 0$ for all n: by (7), U_a, U_m and μ_r positive give $0 < \alpha_n < 1/\cosh(nU_a)$, hence $\cosh(nU_a) - \alpha_n > 0$ for every $n \geq 1$. Its null space contains the constant vector, $\mathbf{Y1} = \mathbf{0}$, because a uniform bore potential drives no flux, and the gauge is fixed by grounding one surface node. The null space reduces to the constants only when the truncation resolves every column, which requires

$$N \geq M_s/2 \tag{13}$$

Definiteness of the coupled system follows without sampling. A reluctance network with positive branch permeances has a weighted-graph-Laplacian nodal matrix; grounding one node makes it symmetric positive definite on a connected network, and $\mathbf{A}_{ss}$ is a principal submatrix of that grounded matrix, hence itself positive definite. Since $-\mathbf{Y}$ is positive semi-definite, the coupled matrix $\mathbf{A}_{ss} - \mathbf{Y}$ is symmetric positive definite for every mesh, and no stabilisation is needed. The rank condition (13) is not required for this: it governs the null space of

Y taken alone. Since rank**Y** $= \min(2N, M_s - 1)$, proved from the spectrum in Sect. III.a, below that threshold the surface block is rank-deficient by $M_s - 2N$ and the coupled system is under-determined on the bore only in the absence of the iron.

Condition (13) fixes the rank; it says nothing about the limit. For large n, $\alpha_n \to 0$ and $g_n \to -\mu_0 n/R_s$, while $(W^c_{nk})^2 + (W^s_{nk})^2 = 4\sin^2(nd_k/2)/(n^2\pi^2)$, so the diagonal entries behave as

$$Y_{kk} \sim -\frac{4\mu_0 L}{\pi}\sum_{n\le N}\frac{\sin^2(nd_k/2)}{n} = -\frac{2\mu_0 L}{\pi}\ln N + O(1) \qquad (14)$$

The sum in (14) diverges logarithmically. This is not a defect of the algebra but a property of the trial space: a piecewise-constant bore potential is discontinuous, its Fourier coefficients decay only as $1/n$, and such a datum does not belong to $H^{1/2}(\Gamma)$, the trace space on which the map is bounded. Until Sect. III settles that question, every statement below holds at fixed truncation.

e. Field recovery and torque

The same coefficients return both field components in the gap without further approximation,

$$B_r(r,\theta) = -\mu_0\sum_{n\ge1}\frac{n\cosh(nv)-\alpha_n\cosh(n(U_a-v))}{r\sinh(nU_a)}(u^c_{s,n}\cos n\theta + u^s_{s,n}\sin n\theta) + B_r^{mag} \qquad (15)$$

$$B_t(r,\theta) = -\mu_0\sum_{n\ge1}\frac{n\sinh(nv)+\alpha_n\sinh(n(U_a-v))}{r\sinh(nU_a)}(u^s_{s,n}\cos n\theta - u^c_{s,n}\sin n\theta) + B_t^{mag} \qquad (16)$$

the magnet contributions B_r^{mag} and B_t^{mag} having the same form with $\alpha_n u_{s,n}$ replaced by β_n, and the field inside the magnet following from the same coefficients as $B^m_{r,n}(r) = -\mu_0\mu_r(n/r)[A_n\cosh(nw) + C_n\sinh(nw)] - \mu_0\mu_r P_n + \mu_0 M_n$. The tangential component is what a radial-branch network cannot produce by itself, and its availability makes a Maxwell-stress torque possible: on a circle of radius r inside the air gap the integral collapses to a Parseval sum,

$$T = \frac{\pi L r^2}{\mu_0}\sum_{n\ge1}(B^c_{r,n}B^c_{t,n} + B^s_{r,n}B^s_{t,n}) \qquad (17)$$

III. TRACE CONFORMITY OF THE CONDENSED OPERATOR

A reluctance network gives each surface node one potential, so the bore datum it hands to the air-gap operator is a staircase. Condensing an exact surface operator onto a staircase is not a matter of resolving the field better: the energy the operator assigns to one column grows without bound as more harmonics are retained, so the number the implementation reports is fixed by where the sum was stopped and not by the geometry, and refining the surface produces another staircase without repairing it. The energy form of the operator on the bore is

$$Y(i,i) = \sum_{n\le N}\hat g_n\,|W_n(i)|^2 \qquad (18)$$

with the assembled admittance $\hat g_n = \pi L R_s g_n$, in henry, growing linearly with n, so finiteness requires $\sum_n n\,|u_n|^2 < \infty$, the $H^{1/2}$ seminorm. Whether the condensation has a limit is therefore decided by the decay of the coefficients of the trial function, and a reluctance network does not choose that function freely. The condition is one of order rather than of geometry, the operator being of order one as the Dirichlet-to-Neumann, Steklov–Poincaré and hypersingular operators are [43], [46]: with a symbol of order α the energy terms of a piecewise-constant basis decay as $n^{\alpha-2}$, so the sum diverges when $\alpha \ge 1$ and converges below it, and the trace argument gives the same threshold, a piecewise-constant function lying in every H^s with $s < 1/2$ while the energy space is $H^{\alpha/2}$; the single-layer potential, whose symbol decays as $1/n$, is the case in which a piecewise-constant density is the conforming choice.

a. The piecewise-constant bore basis and its spectral tail

The indicator of a column of angular width d centred on θ_i has complex Fourier coefficients

$$W_n(i) = \frac{2}{n\pi}\sin\left(\frac{nd}{2}\right)e^{-in\theta_i} \qquad (19)$$

so $|W_n|^2 = O(n^{-2})$ and the energy terms are $\hat g_n|W_n|^2 = O(n^{-1})$. Throughout this section the energy is reported as $-Y(i,i) > 0$, the sign fixed by $g_n < 0$ being dropped so that the tables carry positive entries. The self-energy of one column is then

$$-Y(i,i) = \frac{4\mu_0 L}{\pi}\sum_{n\le N}\frac{1}{n}\sin^2\left(\frac{nd}{2}\right) \qquad (20)$$

which diverges. Splitting the exact kernel into its asymptote and a summable remainder,

$$\hat g_n = \hat g_n^{asym} + \Delta_n, \qquad \hat g_n^{asym} = -\mu_0 L\pi n, \qquad \Delta_n = -\mu_0 L\pi n\left[\frac{\cosh(nU_a)-\alpha_n}{\sinh(nU_a)} - 1\right] \qquad (21)$$

isolates the divergent part. Since $\coth x - 1 = 2e^{-2x}/(1-e^{-2x})$ and $0 < \alpha_n < 1/\cosh(nU_a)$, one has $|\Delta_n| \le 4\mu_0 L\pi n e^{-2nU_a}/(1-e^{-2nU_a})$, so $\Delta_n = O(ne^{-2nU_a})$; with $|W_n| = O(1/n)$ the correction series $\sum_n \Delta_n|W_n|^2$ converges absolutely, and the divergence belongs to $\hat g_n^{asym}$ alone. The departure of the kernel from its asymptote is available in closed form: eliminating α_n from (7) and (9) with $e_a = e^{-2nU_a}$ gives

$$\kappa_n - 1 = \frac{2e^{-2nU_a}[\mu_r\coth(nU_m)-1]}{(1+e_a)+\mu_r(1-e_a)\coth(nU_m)} \qquad (22)$$

so that the rate at which the exact kernel reaches its asymptote is set by the air layer alone, e^{-2nU_a}, while the size of the departure is set by the magnet, through the factor $\mu_r\coth(nU_m) - 1 \to \mu_r - 1 = 0.039$ on this machine; for $\mu_r = 1$ and a thick magnet the correction vanishes identically, and for $\mu_r \ge 1$ one has $\kappa_n \ge 1$ for every n. On the asymptotic kernel the result is in closed form.

Proposition 1 (condensed operator under a piecewise-constant basis). Let the bore be tiled by contiguous columns of widths d_i and centres θ_i, let $\Delta\theta = \theta_j - \theta_i$, and let the condensation be formed on the asymptotic kernel $\hat{g}_n^{asym} = -\mu_0 L\pi n$ truncated at order N. Write $c = \mu_0 L/\pi$, γ for Euler's constant, and define the four arguments

$$a_{1,2} = 1/2\,(d_i - d_j) \pm \Delta\theta, \qquad a_{3,4} = 1/2\,(d_i + d_j) \pm \Delta\theta \tag{23}$$

Then, as $N \to \infty$ at fixed tiling: (i) (entries at two or more columns' distance) if none of $a_1, \dots, a_4$ is a multiple of 2π, which on a contiguous tiling is the case exactly when $|i-j| \geq 2$, the entry converges to the closed form

$$-Y(i,j) = \frac{\mu_0 L}{\pi}\left[-\ln\left|2\sin\frac{a_1}{2}\right| - \ln\left|2\sin\frac{a_2}{2}\right| + \ln\left|2\sin\frac{a_3}{2}\right| + \ln\left|2\sin\frac{a_4}{2}\right|\right] + o(1) \tag{24}$$

(ii) (diagonal) for $i = j$, $d_i = d_j = d$, the self-energy grows without bound as

$$-Y(i,i) = \frac{2\mu_0 L}{\pi}\left[\ln N + \gamma + \ln\left|2\sin\frac{d}{2}\right|\right] + o(1) \tag{25}$$

(iii) (nearest neighbours) for two adjacent columns of a contiguous tiling, $|\Delta\theta| = 1/2\,(d_i + d_j)$, one of a_3, a_4 vanishes and the entry falls without bound; on a uniform tiling of width d,

$$-Y(i,i\pm 1) = -c(\ln N + \gamma) + c\left[\ln|2\sin d| - 2\ln\left|2\sin\frac{d}{2}\right|\right] + o(1) \tag{26}$$

Proof. Write $-Y(i,j) = \frac{4\mu_0 L}{\pi}\sum_{n\leq N}\frac{1}{n}\sin\frac{nd_i}{2}\sin\frac{nd_j}{2}\cos(n\Delta\theta)$, which is (11) on the asymptotic kernel, and expand the product of three circular functions, $\sin A\sin B\cos C = 1/4\,[\cos(A-B+C) + \cos(A-B-C) - \cos(A+B+C) - \cos(A+B-C)]$. With $A = nd_i/2$, $B = nd_j/2$ and $C = n\Delta\theta$ the four arguments are $na_1, \dots, na_4$, so that $-Y(i,j) = c[S_N(a_1) + S_N(a_2) - S_N(a_3) - S_N(a_4)]$ with $S_N(a) = \sum_{n\leq N}\cos(na)/n$. Two classical partial sums decide the limit: for $a \notin 2\pi\mathbb{Z}$, $S_N(a) = -\ln|2\sin(a/2)| + R_N(a)$ with $|R_N(a)| \leq 1/((N+1)|\sin(a/2)|)$ by the Dirichlet test, since the partial sums of $\cos(na)$ are bounded by $1/|\sin(a/2)|$ and $1/n$ decreases to zero; and for $a \in 2\pi\mathbb{Z}$, $S_N(a) = \sum_{n\leq N} 1/n = \ln N + \gamma + 1/(2N) + O(N^{-2})$. For (i), all four arguments avoid $2\pi\mathbb{Z}$ and the four logarithms give (24). On a contiguous tiling, uniform or not, the centres of two adjacent columns are separated by $|\Delta\theta| = 1/2\,(d_i + d_j)$, so one of a_3, a_4 vanishes, one series is the harmonic series and (iii) follows; that is not a degenerate corner to be set aside but the generic case of the two largest off-diagonal entries of every row. On the diagonal $a_1 = a_2 = 0$, so two of the four series are the harmonic series and the remaining two contribute $\ln|2\sin(d/2)|$, which gives (ii). ▫

Corollary 1 (second-difference structure and spectrum). On a uniform tiling of width $d = 2\pi/M_s$ the three closed forms are one formula; of the statements below, (28) with its consequences (a) and (b) holds on any contiguous tiling (Remark 3), while (27) and the spectrum (c) require uniformity. With $S_N(k) = \sum_{n\leq N}\cos(nkd)/n$,

$$-Y(i,i+k) = -c[S_N(k-1) - 2S_N(k) + S_N(k+1)] \tag{27}$$

and since $\ln N$ enters only through $S_N(0) = \ln N + \gamma + o(1)$, the divergent part of the condensed matrix is a periodic second difference,

$$-\mathbf{Y}_N = c\ln N\,\Delta_h + O(1) \tag{28}$$

with Δ_h the periodic second-difference matrix of stencil $(-1, 2, -1)$. Consequently: (a) the row sums of the divergent part vanish, consistently with $\mathbf{Y1} = \mathbf{0}$, which holds at every truncation because each projection W_n, $n \geq 1$, annihilates the constant vector; (b) Δ_h is positive semi-definite, so the divergent part alone respects the negative semi-definiteness that (11) gives $\mathbf{Y}$ at every N; (c) $-\mathbf{Y}$ being circulant, its eigenvalues are

$$\lambda_m = \varepsilon_m \frac{2\mu_0 L M_s}{\pi}\sum_{\substack{n\leq N \\ n\equiv \pm m\ (\mathrm{mod}\ M_s)}}\frac{\kappa_n}{n}\sin^2\left(\frac{\pi n}{M_s}\right), \qquad \varepsilon_m = 2 \text{ for } m \in \{0, M_s/2\},\ \varepsilon_m = 1 \text{ otherwise} \tag{29}$$

on the exact kernel, so that $\lambda_0 = 0$ exactly at every N, $\lambda_m > 0$ if and only if some $n \leq N$ satisfies $n \equiv \pm m$ (mod M_s), which gives $\mathrm{rank}\mathbf{Y} = \min(2N, M_s - 1)$ and the rank condition (13) without a numerical experiment, and $d\lambda_m/d(c\ln N) \to 4\sin^2(\pi m/M_s)$, the eigenvalues of Δ_h.

Proof. On a uniform tiling $a_{1,2} = \pm kd$ and $a_{3,4} = (1 \pm k)d$, so (24) reads $c[2S_N(k) - S_N(k+1) - S_N(k-1)]$ by the evenness of S_N, which is (27); it also contains (25) at $k = 0$ and (26) at $k = \pm 1$. The second-difference stencil applied to the sequence $S_N(k)$ places $\ln N$ at $k = 0$ with weight $+2$ and at $k = \pm 1$ with weight -1, which is (28). For (c), the entries $Y(i,j)$ depend on $i - j$ only, through $\cos(nd(i-j))$, so $-\mathbf{Y}$ is circulant and its eigenvectors are the discrete Fourier modes; the eigenvalue of mode m is $\sum_j(-Y)(0,j)e^{-2\pi imj/M_s}$, and $\sum_j\cos(2\pi nj/M_s)e^{-2\pi imj/M_s}$ equals $M_s/2$ for each of the congruences $n \equiv m$ and $n \equiv -m$, both met at once when $m \in \{0, M_s/2\}$, which gives (29) with $\hat{g}_n = -\mu_0 L\pi n\kappa_n$. Between N and $2N$ the terms added to λ_m are those with $n \equiv \pm m$ in $(N, 2N)$, about $2N/M_s$ of them, each with $\sin^2(\pi n/M_s) = \sin^2(\pi m/M_s)$ and $\kappa_n \to 1$, so the increment is $c\ln 2 \cdot 4\sin^2(\pi m/M_s)$ asymptotically. ▫

The divergent term is therefore not an isotropic shift but a stiffness acting like $-h^2\,\partial_\theta^2$ on the variation of the bore potential, the one thing a piecewise-constant basis cannot represent. Three remarks fix the scope of the proposition.

Remark 1 (exact kernel). Equations (24)–(26) hold exactly for $\hat{g}_n^{asym}$. For the exact kernel of (9) the divergence and the convergence are unchanged by (21); the additive constants acquire the correction $\sum_n \Delta_n W_n(i)\overline{W_n(j)}$, finite, independent of N once $nU_a \gg 1$, and measured in Sect. VI.a to be 2.4307×10^{-11} H on the diagonal of this machine, 0.038 % of the diagonal at $N = 10^3$ and 0.008 % at $N = 10^7$. By (22) the diagonal correction is $cd^2\sum_n n\,(\kappa_n - 1)[1 + O(d^2)]$ with $\sum_n n\,(\kappa_n - 1) = 51.23$ on this annulus, so it scales as $c(d/U_a)^2$ and becomes material only for a thin gap or a coarse tiling; the spectral formula (29) is written on the exact kernel and needs no such correction. Because the additive constant $\gamma + \ln|2\sin(d/2)|$ equals -4.539 for $d = 6$ mrad and its share decays only as $1/\ln N$, the slope is read from the increment per decade, $(2\mu_0 L/\pi)\ln 10$, or per doubling, $(2\mu_0 L/\pi)\ln 2$, and not from a normalised total.

Remark 2 (non-uniform remainder). The $o(1)$ terms are not uniform in the arguments: the remainder of $S_N(a)$ is $O(1/(N|\sin(a/2)|))$, so the closed forms are fixed-tiling statements, quantitative when $Nd \gg 1$. Section III.e examines the other limit, in which the truncation is tied to the tiling and Nd never grows. The remainder is oscillatory, not monotone, which the converging off-diagonal entry of Sect. VI.a exhibits.

Remark 3 (the divergence is the energy of the jumps; any contiguous tiling). Let u be piecewise constant on a contiguous tiling of arbitrary widths, with jumps J_k at the junctions ϕ_k, so that cyclically $\sum_k J_k = 0$. Then $u' = \sum_k J_k\, \delta(\theta - \phi_k)$ in the sense of distributions, $in\hat{u}_n = (2\pi)^{-1} \sum_k J_k\, e^{-in\phi_k}$, and the energy of the condensation truncated at N on the asymptotic kernel is exactly

$$a_N(u,u) = c[H_N \textstyle\sum_k J_k^2 + \sum_{k\neq l} J_k J_l S_N(\phi_k - \phi_l)], \qquad H_N = \sum_{n\leq N} \frac{1}{n} \tag{30}$$

where each cross term converges by the Dirichlet-test bound of the proof above. Hence $a_N(u,u) = c\ln N \sum_k J_k^2 + O(1)$: the divergent part of the condensed energy is $(\mu_0 L/\pi)\ln N$ times the sum of the squared jumps of the bore datum, the truncated $H^{1/2}$ seminorm of a step function. Since $\sum_k J_k^2 = \mathbf{U}^\top \Delta_h \mathbf{U}$ whatever the widths, (28) and its consequences (a) and (b) hold on every contiguous tiling; only (27) and the circulant spectrum (29) need uniformity. For one column indicator, $J = (+1, -1)$, (30) returns the $2c\ln N$ of (25); for two adjacent columns of unequal widths it gives $-Y(i,j) = -c(\ln N + \gamma) + c\,[\ln|2\sin\frac{d_i + d_j}{2}| - \ln|2\sin\frac{d_i}{2}| - \ln|2\sin\frac{d_j}{2}|] + o(1)$, which reduces to (26) at $d_i = d_j$. The identity (30) was checked on a random twelve-column non-uniform tiling to 10^{-15}; the hat remedy of Sect. III.b is, in these terms, exactly the removal of the jumps.

None of this is new as analysis: the mapping properties of the Steklov–Poincaré operator between $H^{1/2}(\Gamma)$ and $H^{-1/2}(\Gamma)$, and the requirement that a Galerkin trial space be a subspace of the energy space, are standard [42]–[44]. What is new is that, within the reluctance-network and air-gap-element literature, the trial space a reluctance network imposes has not been checked against that requirement, and that the check fails: of the records examined over 1986 to 2026, none states the trial space in which its air-gap operator is condensed and none tests it. This is a defect of conformity, not of resolution: refining the bore produces another function outside the space.

b. The piecewise-linear basis restores absolute convergence

The repair follows from the diagnosis. A continuous piecewise-linear hat function of half-width d centred on a node lies in $H^{1/2}(\Gamma)$ and remains one degree of freedom per surface node, its support spanning two columns instead of one. Its coefficients are

$$W_n = \frac{4}{\pi n^2 d} \sin^2\left(\frac{nd}{2}\right) e^{-in\theta_i} \tag{31}$$

so $|W_n|^2 = O(n^{-4})$, the energy terms are $O(n^{-3})$, and the residual tail is bounded by $\sum_{n>N} n^{-3} \sim 1/(2N^2)$. Quantitatively, on the asymptotic kernel the terms are $\frac{16\mu_0 L}{\pi d^2}\frac{\sin^4(nd/2)}{n^3}$, whose mean over the oscillation is $\frac{6\mu_0 L}{\pi d^2 n^3}$, so the tail beyond N is $3\mu_0 L/(\pi d^2 N^2)$ and the increment between N and $2N$ is $3/4 \cdot 3\mu_0 L/(\pi d^2 N^2)$. Truncation becomes a choice of precision instead of a source of bias, and the bound is quantitative: on the released sweep of Sect. VI.b the increment of the hat self-energy between N and $2N$, multiplied by N^2, reaches $3/4 \cdot 3\mu_0 L/(\pi d^2) = 8.7749 \times 10^{-4}$ H to within 0.00009 %, with no constant fitted.

The limit itself is in closed form. On the asymptotic kernel the hat self-energy is $16c \sum_n d \sin^4(nd/2)\cos(nkd)/(nd)^3$, a Riemann sum whose limit as $d \to 0$ at free truncation is the integral $T(k) = 16\int_0^\infty \sin^4(x/2)\cos(kx)x^{-3}dx$; writing the energy form as the single-layer form of the derivatives and integrating the logarithmic kernel over two-unit intervals gives

$$T(k) = 1/2\,[G(k-2) - 4G(k-1) + 6G(k) - 4G(k+1) + G(k+2)], \qquad G(t) = t^2\ln|t| \tag{32}$$

so that $-Y_{hat}(i, i+k)/c \to T(k)$ with $T(0) = 4\ln 2 = 2.772589$, $T(1) = 1/2\,(9\ln 3 - 16\ln 2) = -0.601422$, $T(2) = 28\ln 2 - 18\ln 3 = -0.366900$ and $T(k) \sim -k^{-2}$; the finite-d sums reproduce these values to six decimals at $M_s = 4320$, and the released hat self-energy of Sect. VI.b, 3.662096×10^{-8} H $= 2.7743\, c$, sits 0.06 % above $4c\ln 2$, the difference being the exact-kernel correction of Remark 1 and the finite width. Equation (32) is the Galerkin matrix of the half-space Dirichlet-to-Neumann map on unit hats, which is what the conforming condensation converges to. Dividing the tail by that limit gives the rule an implementer needs: the relative truncation error of the hat self-energy is $3/(4\ln 2\,(Nd)^2)$, so a target ϵ is guaranteed by $Nd \geq 1.040/\sqrt{\epsilon}$, that is $N \geq 0.166 M_s/\sqrt{\epsilon}$; the rank minimum $N = M_s/2$ leaves a relative tail of 15 % and $N = M_s$ of 2.4 %, the rule is quantitative from $N \geq 4M_s$ on, and it requires $N \geq 17\,880$ for $\epsilon = 10^{-4}$ at $M_s = 1080$, against 17 874 read from the released sweep. It bounds the self-energy and not a machine output, which converges far faster on this machine (Sect. VI.b).

c. An error estimate for the conforming condensation

The bore is a circle, so the domain of the operator has no corner; the tooth-tip corner belongs to the stator iron and enters only through the regularity of the datum. On $V = H^{1/2}(\Gamma)/\mathbb{R}$ write $a(u, v) = \langle Su, v\rangle = \sum_{n\geq 1} (-\hat{g}_n)\,(u_n^c v_n^c + u_n^s v_n^s)$, the energy of the harmonic extension into the annulus, with S the Steklov–Poincaré operator whose symbol is (9). Since $0 < \alpha_n < 1/\cosh(nU_a)$ and $\coth x - 1/(\sinh x \cosh x) = \tanh x$, one has $\tanh(nU_a) \leq$

$\kappa_n \leq \coth(nU_a)$ and, by monotonicity, $\tanh U_a \leq \kappa_n \leq \coth U_a$ for every $n \geq 1$. The energy form is therefore equivalent to the $H^{1/2}$ seminorm of the trace,

$$\tanh(U_a)|u|^2_{H^{1/2}} \leq \frac{a(u,u)}{\mu_0 L\pi} \leq \coth(U_a)|u|^2_{H^{1/2}}, \qquad |u|^2_{H^{1/2}(\Gamma)} = \sum_{n\geq 1} n\,(|u^c_n|^2 + |u^s_n|^2) \tag{33}$$

with constants that depend on the air layer alone: on this machine κ_n falls from 7.4607 to within one part in a million of unity by $n = 181$. By (22), $\kappa_n \geq 1$ whenever $\mu_r \geq 1$, so on a magnet layer of recoil permeability at least unity the lower bound in (33) may be replaced by 1; only the upper constant degrades as $U_a \to 0$, $\coth U_a \sim 1/U_a$, the thin-gap regime, which lies outside the present study. Equation (11) can then be read for what it is, $Y_{ij} = -a_N(\psi_i, \psi_j)$, minus the Galerkin stiffness matrix of the form truncated at N on the basis $\{\psi_i\}$, which an independent assembly reproduces to 3.021×10^{-14} in the hat basis and 2.046×10^{-14} in the piecewise-constant one, against an admissibility threshold of 10^{-12} fixed before the check. The model problem for which an estimate can be proved is the condensation alone: given a flux datum $f \in H^{-1/2}(\Gamma)$ with $\langle f, 1\rangle = 0$, find $u \in V$ such that $a(u, v) = \langle f, v\rangle$ for all $v \in V$; the coupled machine problem, in which f is itself produced by the iron network, is not of this form.

Proposition 2 (conforming condensation). Let $V_h \subset V$ be the space of continuous periodic piecewise-linear functions on the uniform tiling of M_s columns, $h = 2\pi/M_s$, and let $u_h \in V_h$ be the Galerkin solution of the untruncated form, $a(u_h, v_h) = \langle f, v_h\rangle$ for all $v_h \in V_h$. Then u_h is the a-orthogonal projection of u onto V_h, so $\| u - u_h \|_a = \inf_{v_h \in V_h} \| u - v_h \|_a$, and for $u \in H^s(\Gamma)$, $1/2 < s \leq 2$,

$$\| u - u_h \|_a \leq C_1 h^{s-1/2}|u|_{H^s(\Gamma)}, \qquad C_1 = C_I\sqrt{\mu_0 L\pi\coth(U_a)} \tag{34}$$

with C_I the constant of the $H^{1/2}$ interpolation estimate for periodic piecewise-linear functions, independent of h, of N and of rotor position.

Proof. Conformity holds because a continuous piecewise-linear function has coefficients $O(n^{-2})$, so $\sum n|u_n|^2 < \infty$; the form is symmetric and coercive on V by (33), so Céa's lemma applies with constant one in the energy norm and u_h is the best approximation, and the standard $H^{1/2}$ interpolation estimate for piecewise-linear functions on a closed curve [43], [44], $\inf_{v_h} |u - v_h|_{H^{1/2}(\Gamma)} \leq C_I h^{s-1/2}|u|_{H^s(\Gamma)}$, combined with the upper bound of (33) gives (34). The L^2 rate follows by duality: the dual problem $a(w, v) = (u - u_h, v)_{L^2(\Gamma)}$ has $|w|_{H^1(\Gamma)} \leq C \| u - u_h \|_{L^2(\Gamma)}$ because the symbol is bounded above and below by multiples of n, and Galerkin orthogonality with the interpolation estimate at $s = 1$ gives $\| u - u_h \|_{L^2(\Gamma)} \leq Ch^{1/2} \| u - u_h \|_a \leq C' h^s |u|_{H^s(\Gamma)}$, one half-order better than (34) [54]. ▫

The archived condensation uses the form and the source truncated at N, and under the locked chain $N = \lfloor M_s/2 \rfloor$ of Sect. III.e the truncation is tied to the tiling, so the question is whether (34) survives it. Two statements answer it. First, no operator-norm bound on the truncation term with a constant independent of the tiling exists: on the uniform tiling both a and a_N are circulant on V_h, hence simultaneously diagonal in the discrete Fourier modes of the nodal vector, with eigenvalues $\lambda_r(\infty)$ and $\lambda_r(N)$ given by the hat analogue of (29), and the consistency term of Strang's first lemma is exactly

$$\epsilon_N := \sup_{v_h, w_h \in V_h} \frac{|a(v_h, w_h) - a_N(v_h, w_h)|}{\|v_h\|_{a_N}\|w_h\|_{a_N}} = \max_r \frac{\lambda_r(\infty) - \lambda_r(N)}{\lambda_r(N)} \tag{35}$$

which on the asymptotic kernel depends on N/M_s alone up to terms in $1/M_s$: $\epsilon_N = 109$ % at the lock at $M_s = 1080$, attained at $r = M_s/2 - 1$, whose mirrored alias $n = M_s - r$ is not retained, and tending to $7/4\ \zeta(3) - 1 = 110$ % as $M_s \to \infty$; $7/8\ \zeta(3) - 1 = 5.18$ % at $N = M_s$; and 1.42 %, 0.37 %, 0.093 % at $N = 2M_s$, $4M_s$, $8M_s$, that is $\propto (M_s/N)^2$. It does not vanish with h at fixed N/M_s, which is why no h-independent estimate of the truncated form in the operator norm is claimed; for the piecewise-constant basis $\lambda_r(\infty) = \infty$ and ϵ_N is infinite. Second, the solution nevertheless converges at the rate of (34), because the deficit lives on the aliased modes only.

Proposition 2′ (locked conforming condensation). Let $u^N_h \in V_h$ solve $a_N(u^N_h, v_h) = \langle f_N, v_h\rangle$ for all $v_h \in V_h$, with form and source truncated at the same $N \geq \lfloor M_s/2 \rfloor$, in particular at the lock $N = \lfloor M_s/2 \rfloor$ of the archived chain. Then $a_N(v_h, v_h) \geq \beta_h a(v_h, v_h)$ on V_h with $\beta_h = \min_{1\leq r\leq M_s-1} \lambda_r(N)/\lambda_r(\infty) > 0$, $\beta_h \to 4/(7\zeta(3)) = 0.4754$ as $h \to 0$ (0.478 at $M_s = 1080$), and $\beta_h = 0$ for $N < \lfloor M_s/2 \rfloor$, so that the rank condition (13) is also the ellipticity threshold of the truncated hat form; and for $u \in H^s(\Gamma)$, $1/2 < s \leq 2$,

$$\| u - u^N_h \|_a \leq (1 + 2\beta_h^{-1/2})C_1 h^{s-1/2}|u|_{H^s(\Gamma)} \tag{36}$$

Proof. Since $\langle f_N, v_h\rangle = a_N(u, v_h)$, u^N_h is the a_N-orthogonal projection of u onto V_h and $\| u - u^N_h \|_{a_N} \leq \| u - I_h u \|_{a_N} \leq \| u - I_h u \|_a$ for the nodal interpolant $I_h u$; on V_h the norms satisfy $\|\cdot\|_a \leq \beta_h^{-1/2} \|\cdot\|_{a_N}$, so $\| I_h u - u^N_h \|_a \leq 2\beta_h^{-1/2} \| u - I_h u \|_a$, and the triangle inequality with Proposition 2 gives (36). For β_h: in the Fourier mode r the ratio $\lambda_r(N)/\lambda_r(\infty)$ equals $\sum_{n\leq N,\, n\equiv\pm r} \kappa_n\, n^{-3} / \sum_{n\equiv\pm r} \kappa_n\, n^{-3}$, the factor $\sin^4(\pi r/M_s)$ of (31) being common to the class; it is smallest at $r = M_s/2 - 1$, where the retained set reduces to r itself while the lost mirror $M_s - r = r + 2$ weighs almost as much, and tends there to $1/(2\sum_{k \text{ odd}} k^{-3}) = 4/(7\zeta(3))$; for $N < \lfloor M_s/2 \rfloor$ the classes $N < r < M_s - N$ are empty. With an untruncated source the same order $h^{s-1/2}$ follows from Strang's lemma [54] at the interpolant, the aliased coefficients of $I_h u$ beyond N carrying $\sin^4(\pi r/M_s) \leq (\pi r/M_s)^{2s}$ against the H^s-stability of trigonometric interpolation for $s > 1/2$ [55], [56]. ▫

The lock therefore does not degrade the rate; it changes the constant, by a factor of at most $1 + 2/\sqrt{0.475} = 3.9$, and it changes the matrix: on a single hat the truncated form at the lock retains only 84.6 % of the self-energy, the locked hat matrix converging as $d \to 0$ to $T_{lock}(0) = 16\int_0^\pi \sin^4(x/2)x^{-3}dx = 2.3469$ in units of c instead of the $4\ln 2 = 2.7726$ of (32). Both locked chains thus converge to definite matrices that are not the Galerkin matrix of the continuous form; only the free-truncation hat chain converges to it. The deficit sits on the roughest nodal modes, which a datum in H^s does not excite at leading order, which is why the released sweep of Sect. VI.b moves the hat fundamental by only 0.023 %. On the smooth-bore benchmark of Sect. VI.b, where the trace is known in closed form, the measured order in the energy norm is 1.50 against the 3/2 that (34) predicts at $s = 2$, 2.01 in L^2 against the 2 of the duality estimate, and 1.50 under the lock, the 3/2 of (36), the three being the slopes over the last doubling of a five-tiling sweep, $M_s = 180$ to 2880, with least-squares fits over the whole sweep of 1.5362, 2.0897 and 1.5495; the locked and the free rates are the same number, 1.5027 against 1.5026, so the lock degrades the guarantee and not the rate. An independent model-problem computation gives energy rates 1.500 and 0.671 for a smooth and a corner datum, identical with and without the lock, and L^2 rates 2.000 and 1.171. The piecewise-constant basis admits no statement of this kind: its discrete solution is not in V, its energy is not finite, and the same trace measured there grows as $3.276 \times 10^{-6}\ln N$ with increment ratios settling on 0.99998 over ten doublings.

On the machine itself the datum is not smooth: the tooth tip is sharp and the opening a parallel-sided channel, so the air sector is 268.35° and $\lambda = \pi/\omega = 0.6708$ [49], [50]; the trace lies in $H^{\lambda+1/2-s}$ and the order of (34) falls to $h^{0.67}$, which is the a priori reason why the slot sidebands and the synchronous inductance do not converge under refinement (Sect. VII.c). The estimate bounds the condensation and nothing else: refining h changes the node set and with it the iron matrix, and no continuous problem exists of which a reluctance network is a consistent approximation, so no bound on a machine quantity follows from (34) and none should be sought.

d. A diagnostic that needs neither the closed form nor the operator

Let $Q(N)$ be any output of the condensed model and $\Delta_k = Q(2^k N_0) - Q(2^{k-1}N_0)$. A logarithmic tail contributes the same amount at each doubling, so $\Delta_{k+1}/\Delta_k \to 1$; a symbol of order $\alpha > 1$ makes the tail algebraic in N and gives $\Delta_{k+1}/\Delta_k \to 2^{\alpha-1}$; geometric convergence with ratio ρ gives $\Delta_{k+1}/\Delta_k \to \rho$. What separates the regimes is therefore whether the limit is at least one or strictly below it, and the criterion is the limit of the sequence and not the value of any one ratio, since a quantity carrying a logarithmic tail on top of a convergent transient approaches unity from below. The test needs only the ability to run the same sum twice. Carried unchanged to the exterior Helmholtz Dirichlet-to-Neumann map of a circle, $\Lambda_n = kH_n'(kR)/H_n(kR)$ with H_n the Hankel function of the first kind [37], an operator of the same order and of another physics, it returns the same verdict: at $kR = 1$, 5 and 20 and at $M_s =$ 180, 360 and 720, over eleven doublings at fixed tiling, the last ratio is 1.00000 in the piecewise-constant basis and 0.25000 in the hat basis, and the stencil of the divergent term in units of the logarithmic step is +2.0000, −1.0000, −0.0000, the periodic second difference of Corollary 1 on another operator; no other statement of this paper rests on that computation.

Three runs are not always enough, and the machine validated here is a counterexample. There the first three ratios are 0.937, 0.845 and 0.872: they fall before they rise, and a sweep stopped at the third would be read as convergence. Eight further doublings show the ratios climbing monotonically to 0.923624 (Sect. VI.b). That value is still below unity, which on a rising sequence bounds the limit from below rather than fixing it; when the first ratios are not monotone the diagnostic should therefore be carried until they are, or applied to a quantity whose limit the theory fixes, here the condensed self-energy, whose increment per doubling is $(2\mu_0 L/\pi)\ln 2$ and which is unambiguous from the third doubling on.

e. Truncation–tiling locking on the test machine

The machine validated here shows no drift, and the reason is not the one the geometry suggests: by (22) the kernel reaches its asymptote at the rate e^{-2nU_a}, in which the magnet thickness does not appear, so with $U_a = 0.02926$ the tail installs itself from $n \approx 34$, against $n \approx 330$ for a bare gap of logarithmic thickness 3×10^{-3}, earlier on the thicker annulus and not later. What protects this machine is the rank condition itself. Under $N = \lfloor M_s/2 \rfloor$ the divergent bracket is held stationary,

$$\ln N + \gamma + \ln|2\sin\tfrac{d}{2}| \to \ln\left(\tfrac{M_s}{2}\right) + \ln\left(\tfrac{2\pi}{M_s}\right) + \gamma = \ln\pi + \gamma \quad (37)$$

so the truncation cannot grow independently of the tiling. That locking is a property of this chain and not of the formulation: holding the tiling and letting the truncation run free makes the defect appear in the outputs of the model (Sect. VI.b), and any implementation in which the truncation is set independently of the surface tiling, whether by a resolution target or by an elimination that reduces the surface unknowns once the operator has been assembled, inherits that behaviour without having chosen it.

The same lock freezes the expansion behind the closed forms. Under $N = \lfloor M_s/2 \rfloor$ the product Nd tends to π at every tiling, so the parameter in which (25) and (26) are asymptotic never grows: measured on the exact kernel over a factor of thirty-two in tiling, $M_s = 540$ to 17 280, the summed diagonal sits between −3.86 % and −4.27 % from (25) and the summed first neighbour between +16.32 % and +16.49 % from (26), both gaps saturating instead of closing, while releasing the truncation at $M_s = 1080$ collapses them to +0.047 % and −0.001 % by $Nd \approx$ 31. The closed forms are correct and are evaluated by the locked chain outside the regime in which they are quantitative. What the locked chain converges to can be stated exactly, and it is neither the continuous operator nor the closed forms.

Proposition 3 (limit of the locked piecewise-constant operator). Let $M_s \to \infty$ with $N = \lfloor M_s/2 \rfloor$ and $d = 2\pi/M_s$, so that $Nd \to \pi$, and let $\sigma(0) = \gamma$, $\sigma(k) = \mathrm{Ci}(k\pi) - \ln(k\pi)$ for $k \geq 1$, $\sigma(-k) = \sigma(k)$, with Ci the cosine integral [57]. Then on the asymptotic kernel, for every fixed $k \geq 0$,

$$-\frac{Y(i,i+k)}{c} = L(k) + \frac{2(-1)^k}{N} + O(N^{-2}), \qquad L(k) = -[\sigma(k-1) - 2\sigma(k) + \sigma(k+1)] \tag{38}$$

so that $L(0) = 2[\gamma + \ln\pi - \mathrm{Ci}(\pi)] = 3.296555$, $L(1) = -[\gamma + \ln(\pi/2) - 2\mathrm{Ci}(\pi) + \mathrm{Ci}(2\pi)] = -0.858902$, $L(2) = -0.417092$, $L(k) = O(k^{-2})$ and $\sum_k L(k) = 0$; the same limits hold on the exact kernel of (9), whose entries carry in addition the correction $cd^2 \sum_n n\,(\kappa_n - 1)\cos(nkd)$ of Remark 1, which vanishes as M_s^{-2} under the lock.

Proof. Under the lock $S_N(kd) = S_N(k\pi/N)$ for M_s even; for M_s odd replace π by $\pi(1 - 1/M_s)$, which changes nothing in the limit. Write $S_N(k\pi/N) = H_N - \frac{1}{N}\sum_{n=1}^{N} f_k(n/N)$ with $f_k(x) = (1 - \cos k\pi x)/x$, analytic on [0,1] with $f_k(0) = 0$. The Euler–Maclaurin formula for the right-endpoint rule gives $\frac{1}{N}\sum_{n=1}^{N} f_k(n/N) = \int_0^1 f_k + [f_k(1) - f_k(0)]/(2N) + O(N^{-2}) = \mathrm{Cin}(k\pi) + [1 - (-1)^k]/(2N) + O(N^{-2})$, with $\mathrm{Cin}(z) = \int_0^z (1 - \cos t)\, t^{-1} dt = \gamma + \ln z - \mathrm{Ci}(z)$; with $H_N = \ln N + \gamma + 1/(2N) + O(N^{-2})$ this is $S_N(k\pi/N) = \ln N + \sigma(k) + (-1)^k/(2N) + O(N^{-2})$ for $k \geq 1$ and $S_N(0) = \ln N + \gamma + 1/(2N) + O(N^{-2})$. Inserting into (27), $\ln N$ cancels and the $1/(2N)$ terms add to $2(-1)^k/N$, which is (38). ▫

The limits are reached as the proof predicts, the asymptotic-kernel entries at the locked tilings of Sect. VI.b agreeing with $L(k) + 2(-1)^k/N$ to $O(N^{-2})$, and they fix the saturations above in closed form: the diagonal deviation from (25) tends to $-\mathrm{Ci}(\pi)/(\ln\pi + \gamma) = -4.278$ % and the first-neighbour deviation from (26) to $+16.51$ %, against -4.27 % and $+16.49$ % measured at $M_s = 17\,280$ on the exact kernel. The locked chain does not stop a divergent sum at an arbitrary place: it converges, as the tiling is refined, to a definite circulant operator whose stencil is the second difference of σ, an operator that is not the Galerkin matrix of any conforming space. That is the precise sense in which the truncation selects a value rather than approximating one, and it is why this machine shows no drift without the closed forms ever being reached; the released sweep of Sect. VI.b, in which N grows at fixed tiling, remains the experiment in which the divergence itself is seen.

IV. COUPLING TO A NONLINEAR RELUCTANCE MESH

a. Polar mesh and the place of the surface block

The stator iron is discretised by a polar mesh of M_s angular columns and L_s radial layers conforming to the slot profile, with the shoe sub-region carrying n_{sh} layers (Fig. 2). Each cell contributes radial and tangential branches whose permeances follow from the local geometry and the material curve, an iron branch carrying $\Delta u = H(B)\ell$ with $B = \Phi/A$; the bore nodes are joined to the first cell layer by a half-branch, iron under a tooth face and air under a slot opening. The tangential branches are what allow slot leakage, and the depth grading $h/3b$ of the classical formula, to emerge instead of being added.

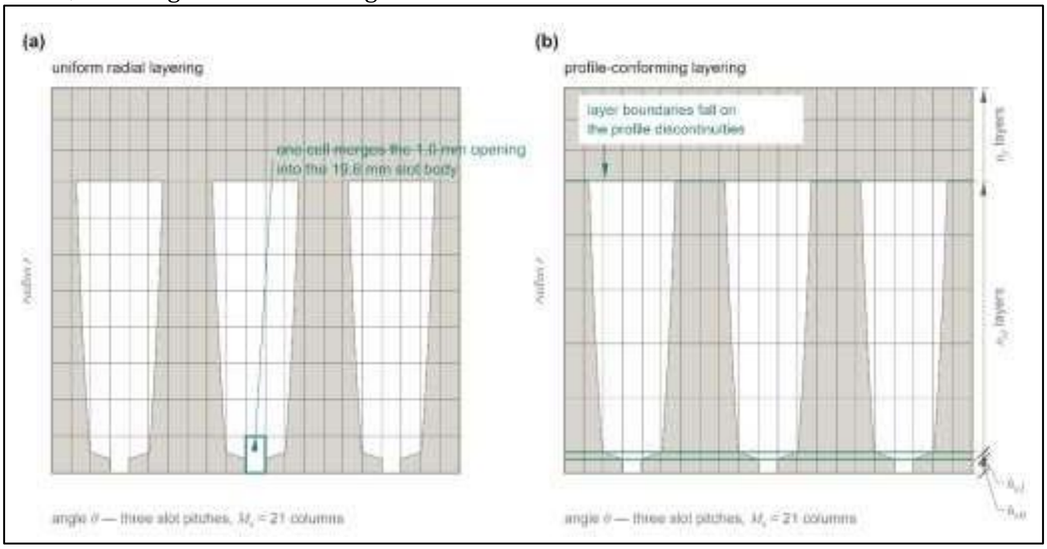

Fig. 2. Radial layering of the stator mesh, developed along the bore.

(a) uniform radial layering, in which one cell merges the 1.0 mm opening into the 19.6 mm slot body; (b) profile-conforming layering, in which layer boundaries are placed on the discontinuities of the slot profile, n_{sh} layers spanning the opening h_{s0} and the wedge h_{s1}, n_{st} the slot body h_{s2} and n_y the yoke. Iron and air are assigned per cell from the true profile, so the tooth width is a solved geometric quantity rather than an arc subtraction.

The surface nodes carry a dense $M_s \times M_s$ block through the air-gap operator, whereas the interior blocks are sparse and are the only ones affected by saturation apart from the half-branches just named. Partitioning the nodal system into surface (s), tooth (t) and yoke (y) unknowns, the surface can be eliminated by a Schur complement,

$$(\mathbf{A}_{tt} - \mathbf{A}_{ts}\mathbf{A}_{ss}^{-1}\mathbf{A}_{st})\mathbf{U}_t + \mathbf{A}_{ty}\mathbf{U}_y = \mathbf{r}_t - \mathbf{A}_{ts}\mathbf{A}_{ss}^{-1}\mathbf{i}_{src} \tag{39}$$

in which $\mathbf{A}_{ss}$ and $\mathbf{A}_{st}$ are invariant with the working point provided the branches touching the surface carry a fixed permeability. Two implementations follow, and the archived chain uses the second. In the lumped chain, where the iron is linear at $\mu_r = 3000$, the whole nodal matrix is independent of rotor position and of the working point, since the operator does not depend on θ_r when one bounding surface is smooth and only the source vector (12) changes; a rotor sweep is then one factorisation of the reduced matrix followed by one back-substitution per position, the cost structure measured in Sect. VI.d. In the meshed chain the shoe cells are saturable, so the half-branches between the bore nodes and the first layer are iron branches under the tooth faces, $\mathbf{A}_{ss}$ and $\mathbf{A}_{st}$ change with saturation and (39) cannot be frozen exactly; the archived solver therefore assembles the full nodal system, dense surface block included, and refactorises it at every Newton iteration, the dense block itself being assembled once per machine and only the iron entries refreshed between iterations.

b. Newton scheme with differential reluctance

The branch relation is inverted in closed form rather than iterated, and the Jacobian uses the differential permeance

$$G_d = \frac{S_b}{\ell}\left(\frac{dH}{dB}\right)^{-1} \tag{40}$$

rather than a numerical derivative. Convergence is measured on the relative nodal residual $\varepsilon = \| \mathbf{f}^{(k)} \| / \| \mathbf{f}^{(0)} \|$, with $\varepsilon < 10^{-9}$ and a limit of thirty iterations for every tabulated chain, and not on the stagnation of B, which is the criterion commonly reported in the reluctance-network literature and which cannot distinguish convergence from an arrested iteration. The step is safeguarded by a backtracking line search of at most twelve halvings on the residual norm, the slope dH/dB is floored at 10^{-9} where the measured curve is flat, and on a rotor sweep the iteration is warm-started from the previous position, which reduces its cost to two or three iterations after the first.

c. Elimination of empirically fitted constants

Three constants that the lumped counterpart requires disappear with the mesh: the slot-opening fringing coefficient, the tangential-leakage factor and the inter-polar leakage factor. Only the first is an air-gap quantity, and the tables of Sect. VI still declare a value for it. In the lumped network the flux entering radially through the slot mouth is carried by a single conductance placed across the opening; the mesh resolves that entry explicitly, through the isthmus and bevel layers and the tangential branches between them, so the parameter is carried through the mesh chain as a declared configuration field and used by no permeance: changing it from 0.325 to 0.750 left the computed slot sideband identical to twelve significant figures, $1.580801250548 \times 10^{-2}$ T in both settings. Two identifications of the same constant show what is being removed: fitted against the finite-element tooth-band amplitudes it comes out at 0.75, fitted against the three lumped field quantities at 0.325, a factor of 2.3 apart, each defensible on its own bench. A coefficient whose value depends on which quantity it is identified against is not a property of the geometry, and that, rather than the count of constants, is what the operator removes.

V. VALIDATION PROTOCOL AND TEST MACHINE

The results of Sect. VI are organised on three levels that answer three different questions, and a statement made at one level is never used as evidence at another. *Level 1, mathematical:* does the computation reproduce what the theory predicts? The objects are the closed forms of Proposition 1, the tail of the hat basis, the spectral formula (29) and the rank condition, each an exact value measured with no free constant. *Level 2, numerical:* are the outputs independent of the parameters that are not part of the physics, the tiling M_s, the layering n_{sh}, the truncation N or N_h, the Newton tolerance, the quadrature of the loss integrals and the conditioning of the reduced system? The objects are dispersions and convergence orders, and where a closed-form solution of the annulus exists it serves as an exact reference that no mesh enters. *Level 3, electrotechnical:* does the operator, inside the machine model, return the field, circuit and terminal quantities as an independent two-dimensional finite-element solution returns them, and does it do better than the closures it replaces? The objects are the deviations of Sect. VI.c, read against the floors that Level 2 establishes and against what the reference can resolve. Six sources of error are separated: the discretisation of the bore tiling and of the iron mesh (Sect. VI.b); the truncation of the harmonic series (Sect. VI.b); the round-off and overflow behaviour of the double-precision kernel, where evaluation through $\sinh(nU_m)$ overflows beyond $nU_m > 710$ and is replaced by a negative-exponent form; the quadrature of the loss integrals, 0.2 % over 181 to 481 rotor positions; the conditioning of the reduced system, a condition number of 8.8×10^4 at the lock falling to 6.8×10^4 under release with no rank loss; and the error of the finite-element reference itself, audited in Sect. VI.c rather than assumed.

The reference is ANSYS Electronics Desktop 2023 R1, Maxwell 2-D, and Table 2 lists the machine data read from its project. Three classes of source feed the comparison and no others: the finite-element project, from which geometry, winding, lamination characteristic, magnet data and loss coefficients are read directly; four solved reference studies, magnetostatic, transient no-load, transient on-load and a speed sweep at constant dc-bus voltage, the magnetostatic studies having used adaptive refinement converged in two and three passes while the transient studies carry the mesh written into the project; and the dated transcripts written by the network runs. The lamination characteristic is the measured 81-point $B(H)$ curve of the M350-50A steel, assigned to both stator and rotor; $\mu_r = B_{rem}/(\mu_0 H_c) = 1.0390$ is derived from the project's two magnet inputs; iron losses use the Bertotti coefficients of the reference itself [58]. Comparisons are made on identically defined functionals at identical locations, flux densities at the mid-gap radius $r = R_s - g/2$, the probe radius of the reference, torque from (17) on a circle inside the air gap, and magnet losses from (42) with zero net current over the magnet cross-section, after one registration established per machine on the flux linkage rather than on the back-electromotive force, since differentiating amplifies the high-order content the registration is meant to align. The effect measure is the signed relative deviation.

Table 2. Data of the test machine, read from the finite-element project; the left pair of columns is geometry, the right winding, materials and drive.

Quantity	Value	Quantity	Value
rated output	750 W	winding factor k_{w1}	0.9514
slots / poles	15 / 14 ($p = 7$)	turns per coil / per phase	152 / 760
stator bore D (mm)	69.356	winding layers / parallel paths	1 / 1
stator outer diameter (mm)	125.0	phase resistance (Ω, 80 °C)	10.2223
mechanical air gap g (mm)	1.000	lamination	M350-50A
active length L (mm)	33.0	stacking factor	0.90
magnet thickness (mm)	3.500 (embrace 0.94)	Bertotti k_h, k_c, k_e	182.455, 1.34676, 0[b]
tooth width (mm)	8.490	magnet	N42UH
slot height $h_{s0}/h_{s1}/h_{s2}$ (mm)	1.00 / 0.50 / 19.60[a]	B_{rem} (T) / H_c (kA/m)	1.2471 / 955.204
slot width $b_{s0}/b_{s1}/b_{s2}$ (mm)	2.00 / 6.70 / 15.03	μ_r / σ (S/m)	1.0390 / 555556
total slot height (mm)	21.10	supply	500 V dc, six-step
stator / rotor yoke (mm)	6.722 / 14.678	inertia (kg m^2) / damping (N m s)[c]	1.0×10^{-3} / 6.07927101854027×10^{-4}
		load torque (N m)	4.8

$$\delta = \frac{x_{MEC} - x_{FEA}}{x_{FEA}} \tag{41}$$

formed on full-precision values and rounded once at display, negative meaning that the network is below the reference; the dispersion of a swept quantity is (max − min)/|mean| over the sweep. Efficiency is compared as a difference in points and evaluated with the reference's own definition, $\eta = P_{out}/(1.02P_{out} + P_{cu} + P_{core} + P_{solid})$, in which P_{out} is the electromagnetic power and 1.02 the reference's flat-rate allowance for friction and windage; this is a comparison functional and not a normative efficiency, and evaluated on the reference's own instantaneous losses it reproduces the solver's efficiency output at every one of its 250 samples to a worst relative deviation of 7.1×10^{-15}.

[a] Slot type tc6, semi-closed with parallel-sided teeth; the parallel-tooth condition is satisfied to 1.7×10^{-6} in the generated profile. [b] The excess-loss coefficient is zero in the project's own material definition, so the Bertotti separation reduces here to hysteresis and eddy currents. [c] The mechanical rows are the reference project's own motion setup, which the network drive model of Sect. VI.c integrates unchanged; the phase resistance is the value the chain uses, 10.222304 Ω, printed at the precision of the project. The magnet resistivity is 1.80×10^{-6} Ω m and the mass density 7650 kg/m^3.

Four commitments govern what may be reported. Every published quantity is bound by a versioned manifest to the dated output it is read from, written after the runs and before the tables were filled; no value is transcribed by hand and no rounded value is the input of a further computation. One quantity is produced by one declared chain, a result that cannot be regenerated is withdrawn rather than kept with a note, and a discrepancy is never reconciled by changing the reference. A quantity is excluded when the reference offers several determinations without one being nominated, and when its value depends on a constant identified against that same reference. And the two comparison axes are kept apart: along the iron axis the closure is held at the operator and the iron discretisation varied (Sect. VI.c); along the closure axis the iron model is held at the lumped network and the closure varied (Table 1). All results of Sect. VI other than the two mesh columns of the no-load comparison of Sect. VI. c use the lumped iron model; no parameter of the meshed chain is adjusted against the reference, the lumped counterpart carries the three fitted constants of Sect. IV.c, and the two models do not share the same winding temperature. Four checks bound the network solution itself: continuity of the radial flux density across the magnet/air interface holds to 4.3×10^{-16} over the orders $n \le 80$ that carry the field; the computed torque is unchanged to the last bit when the Newton tolerance is tightened over four decades; the nodal flux balance closes to between 1.2 and 8.6×10^{-17} Wb across the chains of Sect. VI.c, one part in 10^{13} of the largest branch flux; and wherever a torque discrepancy is reported, the ratio of the sum of absolute terms to the algebraic sum of (17) is formed, so that a physical difference can be separated from cancellation in the Parseval sum.

A numerical reference is not a measurement, so comparing two numerical models bounds their difference and never their common distance from the physical machine; no experimental agreement is asserted anywhere in this paper. Two open-circuit measurements would close the gap: the phase resistance, four-wire at a recorded winding temperature, and the open-circuit line-to-line back-electromotive force at a measured shaft speed, one waveform that tests the magnetisation spectrum (5), the transfer α_n of (7) and the slot modulation carried by g_n at once. Since the integral deviations reported here lie between 0.1 % and 0.35 %, the class required is ≤ 0.2 % on the electromotive force, ≤ 0.1 % on shaft speed and ≤ 0.5 % on winding resistance with the temperature measured to ±2 K; at that class the measurement would discriminate on flux linkage, back-electromotive force and synchronous inductance, but not on the mutual inductance alone, and would say nothing about the sidebands or the cogging torque. The comparison set is reported in full, its twenty-nine quantities being the twenty-nine bars of the synthesis figure of Sect. VI.c, and it includes the quantities on which the operator loses.

VI. Results

Every machine result below is computed in the piecewise-constant surface basis, the non-conforming basis of Sect. III.a. Its diagonal is finite only because the truncation is locked to the tiling by (37); the values are therefore reproducible values of a selected operator and not values of a limit. The hat basis is exercised where the two are compared, in Sect. VI.b, which is what licenses the piecewise-constant readings: carried through this same chain, the conforming basis reproduces the compared quantities to within the dispersion the tiling alone produces. The same locking sets a floor under everything that follows: under the locked chain the tiling dispersion of the fundamental gap flux density is 0.440 % in the piecewise-constant basis and 0.496 % in the hat basis, that of the first slot sideband 26.126 % and 28.514 %, and the tiling alone moves the peak flux linkage by 0.612 %, the phase self-inductance by 1.766 %, the mutual by 2.039 % and the synchronous inductance by 1.777 % in the piecewise-constant basis, and by 0.708 %, 1.964 %, 2.251 % and 1.976 % in the hat basis (Sect. VI.b). A deviation smaller than that floor is reported below as a bound rather than as an agreement. Deviations are formed on full-precision values and rounded once at display.

a. Level 1: the computation against the theory

Algebraic properties of the condensed operator. The condensed bore matrix was symmetric to machine precision, as (11) requires, and negative semi-definite, its null space spanned by the constant vector once $N \geq M_s/2$: at $M_s = 360$ on the exact kernel the rank ran 120, 240, 358, 359 and 359 at $N = 60$, 120, 179, 180 and 360, the rank statement of Corollary 1 and nothing further. The coupled matrix formed with the iron network was symmetric positive definite on every mesh tried, and no stabilisation was applied. The spectral formula (29) reproduces the assembled spectrum to a relative 10^{-15} to 10^{-14} at $M_s = 360$ and 1080, and $d\lambda_m/d(c\ln N)$ approaches the eigenvalues $4\sin^2(\pi m/M_s)$ of Δ_h, the maximum relative deviation of the increment per doubling at $M_s = 1080$ falling monotonically from 8.15 % at $N = 1080 \rightarrow 2160$ to 0.0005 % at $N = 138\,240 \rightarrow 276\,480$.

Proposition 1 verified by direct summation. The diagonal entry was obtained in closed form and verified against its own numerical summation, on the two-layer annulus this paper validates rather than on a bare air gap (Table 3). On the asymptotic kernel the closed form (25) and the summation agree to a relative deviation between 2.936×10^{-7} and 1.373×10^{-6} at $N = 10^7$ over three column widths, 6, 12 and 24 mrad, and the increment per decade settles between 6.0786 and 6.0787×10^{-8} H against the predicted $(2\mu_0 L/\pi)\ln 10 = 6.0788 \times 10^{-8}$ H, with no adjusted quantity anywhere in the comparison. Entries with $|i - j| \geq 2$ converge, as (24) requires: at a separation of 8.3 column widths ($d_i = d_j = 6$ mrad, $\Delta\theta = 50$ mrad) the summed value reaches its closed form -1.9150×10^{-10} H to 2.3×10^{-5} at $N = 10^7$, through relative deviations of 1.052×10^{-1}, 2.554×10^{-1}, 5.460×10^{-2} and 2.260×10^{-4} over the preceding decades, the non-monotone residual being the oscillatory remainder of Remark 2; at the truncation the validated chain uses, $N = 540$ at $M_s = 1080$, they differ from their limits by −43.95 %, +39.79 %, +33.33 % and −4.39 % at $|i - j| = 2$, 3, 5 and 10. On the exact two-layer kernel (Table 3, last column) the increment per decade is the same to the printed resolution, so the divergence belongs to the operator and not to the degeneracy of the layer solution: the correction between the two kernels is a constant of 2.4307×10^{-11} H, acquired by $N = 10^3$ and thereafter identical to the last bit, 0.037767 % of the diagonal at $N = 10^3$ and 0.007951 % at $N = 10^7$; on a bare gap an order of magnitude thinner it would reach a tenth of the diagonal at $N = 10^7$, in the proportion $c(d/U_a)^2$ of Remark 1.

Table 3. Verification of Proposition 1 on the two-layer annulus of the machine validated here: diagonal entry at $d = 6$ mrad; magnet layer of recoil permeability $\mu_r = 1.0390$ followed by the air layer, $U_a = 2.9261 \times 10^{-2}$, $U_m = 1.0973 \times 10^{-1}$, $L = 33.0$ mm.

N	summed $-Y(i,i)$, asymptotic kernel (H)	closed form (25) (H)	rel. dev.	increment per decade (H)	exact two-layer kernel (H)
10^3	6.4338×10^{-8}	6.2541×10^{-8}	2.874×10^{-2}	—	—
10^4	1.2346×10^{-7}	1.2333×10^{-7}	1.051×10^{-3}	5.9121×10^{-8}	1.2348×10^{-7}
10^5	1.8412×10^{-7}	1.8412×10^{-7}	9.523×10^{-6}	6.0657×10^{-8}	1.8414×10^{-7}
10^6	2.4491×10^{-7}	2.4491×10^{-7}	7.692×10^{-6}	6.0792×10^{-8}	2.4493×10^{-7}
10^7	3.0569×10^{-7}	3.0569×10^{-7}	1.373×10^{-6}	6.0786×10^{-8}	3.0572×10^{-7}

The diagonal does not converge, its increment per decade matching the predicted slope $(2\mu_0 L/\pi)\ln 10 = 6.0788 \times 10^{-8}$ H; at $d = 12$ and 24 mrad the relative deviation at $N = 10^7$ is 3.827×10^{-7} and 2.936×10^{-7} and the increment per decade 6.0787×10^{-8} H. The correction of (21) is acquired by $N = 10^3$ and shifts the constant by 2.4307×10^{-11} H without depending on N; the panel is recomputable from (24), (25) and (9) alone.

The hat basis: residual tail against its bound. In the hat basis the energy series converges absolutely: the residual tail beyond truncation fell from 3.4270×10^{-8} H at $N = 10^2$ to 8.6826×10^{-10}, 1.0838×10^{-11}, 1.1003×10^{-13} and 1.0998×10^{-15} H at $N = 10^3$ to 10^6, and its product by N^2 rose through 0.000343, 0.000868, 0.001084 and 0.001100 to settle at 0.001100 H over the last two decades, against the $3\mu_0 L/(\pi d^2) = 1.100 \times 10^{-3}$ H that the tail of (31) imposes at $d = 6$ mrad with no constant fitted. The exact two-layer kernel gives the same tail from $N = 10^3$ on, and the five values are verified by two independent routes at forty digits, which agree to a relative 3×10^{-16}.

b. Level 2: independence from the numerical parameters

What an implementation inherits once the truncation is free. The released sweep plotted in Fig. 3 is the behaviour any implementation inherits once the truncation is no longer tied to the tiling. Holding the tiling at $M_s = 1080$ and letting N_h run over eleven doublings, from 540 to 1 105 920, the fundamental gap flux density drifts monotonically instead of settling, by 0.703 % in the piecewise-constant basis against 0.023 % in the hat basis, while the bracket resumes the growth that (25) predicts, by 442.8 % over the sweep and at a slope of 2.302585 per decade against $\ln 10 = 2.302585$. On the self-energy of a column on the exact two-layer kernel, the quantity Proposition 1 predicts exactly, the piecewise-constant increment per doubling approaches the parameter-free constant $(2\mu_0 L/\pi)\ln 2 = 1.829909 \times 10^{-8}$ H instead of tending to zero, its deviation from that constant falling from $+13.6$ % at the first doubling to -0.00001 % at the last; the hat self-energy settles at 3.662096×10^{-8} H and the product of its increment by N^2 reaches 8.774933×10^{-4} H against the predicted 8.774941×10^{-4} H. The rows beyond $N_h = 8640$ require the overflow-free evaluation of the kernel named in Sect. V, and no rank is lost along the sweep, the reduced matrix of order 1109 having smallest singular value 1.649059×10^{-8} at the largest truncation against 1.277703×10^{-8} at the lock. The locking of (37) holds because the rank condition ties N to M_s, and a chain that sets the truncation for any of the reasons listed in Sect. III.e loses it without having decided to.

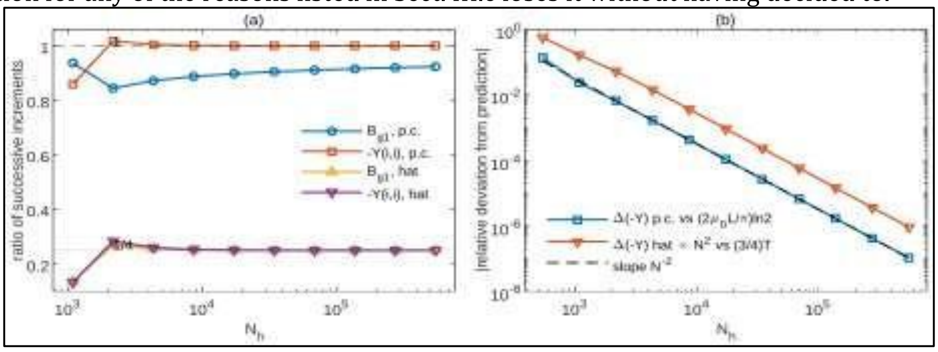

Fig. 3. Convergence diagnostics of the released sweep at $M_s = 1080$, $N_h = 540$ to 1 105 920. (a) Ratio of successive increments. the piecewise-constant curves rise towards unity without settling, the logarithmic signature, while the hat curves sit on 1/4, the value a tail in n^{-3} imposes. (b) Absolute relative deviation of each increment from the constant its basis predicts, with no quantity fitted: both fall as N_h^{-2}, so the two predictions are attained at the same rate and neither is an extrapolation.

The smooth-bore control and an exact reference that no mesh enters. One control removes the machine from the question entirely. Take the annulus of Table 2, with the same operator, radii, magnet, tiling $M_s = 1080$ and truncation sweep, and replace the slotted stator bore by a solid cylinder: there is then nothing on the bore to resolve, and any drift under truncation is attributable to the basis alone. Removing the slot openings alone leaves the bore held by fifteen tooth bodies at fifteen different potentials, with a largest step between adjacent columns of 0.965 of the whole range; tying the bore to a single iron node removes the jumps, and the largest step falls to 0.064 of the range. Over $N_h = 540$ to 17 280 with the openings removed, the piecewise-constant fundamental drifts by 8.446×10^{-4} % and the hat fundamental by 3.170×10^{-5} %, a ratio of 26.6; on the equipotential ring the hat fundamental is constant to 42 units in the last place of double precision while the piecewise-constant one still drifts by 5.594×10^{-8} %, 2 768 137 units in the last place. Geometry, operator and tiling being identical across the three bores, the residual drift is projection error and nothing else. The smooth-bore annulus also has a closed-form solution: with a bore of finite permeability $\mu_I = 3000$ it gives $B_{g1} = 1.0987807$ T against 1.0989210 T for a bore taken infinitely permeable, two independent implementations and the published closed form of [52] agreeing to a relative 2.6×10^{-15} over thirty harmonics. Measured against it under the locked truncation, both bases converge at order two in the column width, the deviation falling over four tilings from 7.1×10^{-6} % to 1.1×10^{-7} % in the piecewise-constant basis and from 1.4×10^{-5} % to 2.2×10^{-7} % in the hat basis; releasing the truncation separates them there as on the machine, the piecewise-constant deviation drifting at $M_s = 1080$ over twenty doublings by 2.3×10^{-7} % in equal increments of 1.15×10^{-8} % per doubling, the logarithmic signature of (25), while the hat deviation moves by 8.5×10^{-13} %. Every figure of this subsection is recomputed independently from (9), (8) and (19)–(31) alone by a deposited script, to a relative 1.8×10^{-13} on the closed-form fundamental.

Table 4. The locked chain over six tilings, $N = \lfloor M_s/2 \rfloor$, in both surface bases: fundamental gap flux density, first slot sideband and the four integral quantities of Sect. VI.c, with the dispersion of each over the six tilings; over the five finest, the coarsest being a tiling the validated chain never uses, the dispersions of the four integral quantities fall to 0.176 %, 0.390 %, 0.453 % and 0.392 % in the piecewise-constant basis and 0.138 %, 0.345 %, 0.400 % and 0.347 % in the hat basis.

Basis	M_s	N	B_{g1} (T)	$\nu = 8$ (T)	λ peak (Wb)	L_a (mH)	M (mH)	L_d (mH)
p.c.	540	270	1.07390	0.021761	0.259990	50.07544	−2.18502	52.26046
p.c.	1080	540	1.07865	0.016944	0.261587	50.97078	−2.23023	53.20100
p.c.	1260	630	1.07755	0.018062	0.261206	50.77264	−2.22015	52.99278
p.c.	2160	1080	1.07793	0.017672	0.261317	50.85949	−2.22458	53.08407
p.c.	4320	2160	1.07759	0.018014	0.261189	50.80404	−2.22177	53.02581
p.c.	8640	4320	1.07743	0.018180	0.261128	50.77613	−2.22035	52.99648
p.c.	dispersion, six tilings		0.440 %	26.126 %	0.612 %	1.766 %	2.039 %	1.777 %
hat	540	270	1.07267	0.023000	0.259531	49.83764	−2.17334	52.01097
hat	1080	540	1.07801	0.017596	0.261379	50.83138	−2.22313	53.05450
hat	1260	630	1.07698	0.018637	0.261018	50.65639	−2.21426	52.87065
hat	2160	1080	1.07759	0.018020	0.261206	50.79041	−2.22107	53.01148
hat	4320	2160	1.07741	0.018195	0.261132	50.76983	−2.22003	52.98986
hat	8640	4320	1.07734	0.018271	0.261099	50.75922	−2.21949	52.97872
hat	dispersion, six tilings		0.496 %	28.514 %	0.708 %	1.964 %	2.251 %	1.976 %

The locked chain separates neither basis, because it measures the tiling transient of the two projections and not the truncation behaviour, which the lock suppresses in both bases by construction; these dispersions are the floors against which the deviations of Sects. VI.c and VII are read. The divergent bracket of (25) is stationary under the lock, at 1.721940, 1.721944, 1.721945, 1.721945 and 1.721946 for $M_s = 540$ to 8640, against $\ln\pi + \gamma = 1.721946$, while the self term moves by −0.21 % over a factor of sixteen in tiling on the asymptotic kernel and −0.4169 % on the exact kernel of (9), the $o(1)$ that (25) discards.

Dispersion under the locked chain and the conforming basis on the machine. Table 4 is the panel most likely to be misread. The hat basis disperses slightly more over the six tilings, 0.496 % against 0.440 % on the fundamental and 28.5 % against 26.1 % on the first sideband, which invites the conclusion that the conforming basis is the worse of the two. It is not what the table measures: under the locked chain the tail that diverges is never summed, the dispersion is the transient of the two projections under tiling refinement, and the whole of the difference is carried by the coarsest tiling, which the validated chain never uses; dropping that one point reverses the ordering, to 0.096 % against 0.113 % on the fundamental and 5.7 % against 7.0 % on the sideband, and the separation of the two condensations on the fundamental falls from 0.115 % at the coarsest tiling to 0.008 % at the finest, first order in the column width. Table 5 carries both bases through the chain of this section, at the tiling that chain uses, against the same finite-element reference: the conforming basis is closer on the fundamental gap flux density, on the first slot sideband and on the peak flux linkage, and farther only on $\nu = 22$, which Sect. VII.c reports as a bound in either basis. None of the four differences is large and none is claimed as an improvement; the theorem costs nothing where the truncation is locked, its gain is the released sweep, and the results below do not depend on which of the two bases carries them.

Table 5. Both surface bases against the finite-element reference, lumped iron network, $M_s = 1260$, $N = 630$.

Quantity	reference	p.c.	δ p.c.	hat	δ hat
B_{g1} (T)	1.074551	1.077547	+0.279 %	1.076981	+0.226 %
$\nu = 8$ (T)	0.019658	0.018062	−8.12 %	0.018637	−5.19 %
$\nu = 22$ (T)	0.032760	0.035238	+7.56 %	0.036196	+10.49 %
λ peak (Wb)	0.258328	0.261206	+1.11 %	0.261018	+1.04 %

The dated run prints nine decimals, 1.077547401, 0.018061876 and 0.035237748 T in the piecewise-constant basis and 1.076980714, 0.018636572 and 0.036195726 T in the hat basis, and its exact-coefficient control agrees with the 2000-point grid evaluation to 4×10^{-16}, so grid aliasing does not enter the comparison.

Coupling to the nonlinear mesh. The Newton scheme built on the differential reluctance reaches a relative nodal residual between 4.6×10^{-13} and 2.3×10^{-12} in eleven to fifteen iterations, measured at four rotor positions of the mesh chain at $M_s = 900$ with two layers in each shoe sub-region, 10 800 unknowns; its last step is quadratic, the relative residual passing at the first of those positions from 1.5×10^{-4} at the tenth iteration to 2.3×10^{-12} at the eleventh. No tolerance between 10^{-6} and 10^{-12} can therefore select a different iterate, and the computed torque varies by at most 1.0×10^{-13} mN m over that range. Successive substitution on the permeability does not compete on the same network: without relaxation its relative residual never falls below 0.70, and with the sub-relaxation of 0.35 used elsewhere in the chain it reaches 1.2×10^{-4} after 500 iterations, eight orders of magnitude above what Newton reaches in fifteen. Every result reported below is a converged solution of the discrete problem, every tabulated chain passing the tolerance 10^{-9} within thirty iterations.

Mesh convergence and the quantity that does not converge. Two refinements of the stator mesh move the same quantity in opposite directions (Table 6). Refining the bore angularly at one shoe layer raised the first slot sideband from −42.3 % to −9.7 % while the fundamental converged from +0.9 % to +0.2 %; refining the shoe radially at fixed angular grid lowered it, reaching −18.8 % under the linear solver at $M_s = 900$, while under Newton on the same meshes the sideband ran from +10.3 % to +23.8 %, so the two solvers bracket the reference from opposite sides. Refining the shoe at $M_s = 900$, the linear peak iron flux density grew from 2.80 T to 3.47 T on a material saturating near 2 T, while the Newton solution stayed between 2.006 T and 2.013 T. The bracket width between the linear and Newton predictions was 41.7 percentage points at one shoe layer and 42.6 at four, and does not close under refinement of the region that should resolve the quantity; the sideband is therefore reported as a bracket. The synchronous inductance does not settle either: it deviates by +0.5 %, +0.2 % and +0.1 % over the first three refinements and by +2.5 % at the finest, a reversal carried by the phase self-inductance itself, which rises from 50.379 to 51.549 mH between the last two grids, so the deviation quoted for it in Sects. VI.c and VIII is its value in the configuration declared for Table 7 rather than the limit of this sequence.

Table 6. Mesh convergence of the coupled model: angular refinement at one layer per shoe sub-region ($n_{sh} = 1$, nine radial layers), and angular sweep at four layers per shoe sub-region ($n_{sh} = 4$, fifteen radial layers, $n_{st} = 4$, $n_y = 3$) with both solvers on identical meshes.

n_{sh}	M_s	unknowns	B_{g1}	L_d	$\nu = 8$, linear	$\nu = 8$, Newton	peak iron B, linear	peak iron B, Newton
1	180	1800	+0.9 %	+0.5 %	−42.3 %	—	2.209 T	—
1	360	3600	+0.4 %	+0.2 %	−19.8 %	—	2.570 T	—
1	540	5400	+0.3 %	+0.1 %	−13.3 %	—	2.699 T	—
1	900	9000	+0.2 %	+2.5 %	−9.7 %	—	2.799 T	—
4	360	5760	—	—	−26.8 %	+10.3 %	2.908 T	1.928 T
4	540	8640	—	—	−21.6 %	+15.0 %	3.191 T	1.979 T
4	900	14400	—	—	−18.8 %	+23.8 %	3.471 T	2.013 T

PMSM 15/14, linear solver at $\mu_r = 3000$, $k_f = 0.325$ (inert in this chain, Sect. IV.c), piecewise-constant basis, rotor at $\theta_r = 0$; deviations against the finite-element reference $B_{g1} = 1.074548$ T, $\nu = 8$ at 0.0196594 T, $L_d = 52.3415$ mH. Read at matched columns, the $n_{sh} = 4$ rows give the radial refinement of the shoe; the bracket quoted in Sects.

VI.b and VII.c comes from the archived sweep that varies the shoe layering from one to four at $M_s = 900$ under both solvers, where its width is 41.7, 42.2, 42.5 and 42.6 percentage points. Sweeping n_{sh} from 1 to 4 against the six published cells leaves a maximum residual of 9.08, 2.78, 0.81 and 0.06 percentage points respectively, so the layering was identified rather than assumed.

c. Level 3: the operator inside the machine model

No-load field, circuit and terminal quantities. The deviations below are reported before the reference has been audited, and Sect. VII.b bounds what they can mean: the uncertainty budget produces no band on any field quantity, so a deviation of a few tenths of a percent on such a quantity is no larger than the reference can resolve and is not a measurement of the model; Table 4 adds a second floor to every compared quantity. Deviations above those two floors are model errors; deviations below them are bounds. Table 7 reports the mesh model at two shoe layerings, its lumped counterpart and the reference.

Table 7. PMSM at no load: the mesh model at two shoe layerings, its lumped counterpart, and the two-dimensional finite-element reference. The three network columns carry the same DtN operator on the bore and differ only in the iron.

Quantity	Mesh $n_{sh}=1$	Mesh $n_{sh}=2$	Lumped	FEA	δ mesh 1	δ mesh 2	δ lumped
B_{g1} (T)	1.07787	1.07908	1.07755	1.07455	+0.31 %	+0.42 %	+0.28 %
$\lvert B_r\rvert$ mean (T)	0.76182	0.76273	0.76147	0.76091	+0.12 %	+0.24 %	+0.07 %
B_r peak (T)	0.98051	0.97536	0.98600	0.99073	−1.03 %	−1.55 %	−0.48 %
B_t rms (T)	0.13755	0.13478	0.14317	0.13326	+3.22 %	+1.14 %	+7.43 %
slot sideband $\nu = 8$ (T)	0.01704	0.01581	0.01806	0.01966	−13.34 %	−19.58 %	−8.12 %
flux line A (Wb/m)	0.005861	0.005868	0.005860	0.005855	+0.11 %	+0.22 %	+0.09 %
flux linkage, peak (Wb)	0.25894	0.25908	0.26121	0.25833	+0.24 %	+0.29 %	+1.11 %
MMF per magnet (A)	761.674	759.329	762.912	769.445	−1.01 %	−1.31 %	−0.85 %
MMF per gap (A)	711.386	711.880	725.064	721.504	−1.40 %	−1.33 %	+0.49 %
MMF dispersion (%)	6.369	5.959	6.810	6.585	−3.27 %	−9.50 %	+3.42 %
phase back-EMF, peak (V)	238.813	238.818	240.877	233.031	+2.48 %	+2.48 %	+3.37 %
six-step envelope (V)	464.556	464.645	468.719	459.918	+1.01 %	+1.03 %	+1.91 %
L_a (mH)	50.379	50.484	50.773	50.209	+0.34 %	+0.55 %	+1.12 %
M (mH)	−2.016	−2.021	−2.220	−2.133	−5.48 %	−5.24 %	+4.09 %
L_d (mH)	52.395	52.505	52.993	52.342	+0.10 %	+0.31 %	+1.24 %
k_r	1.07069	1.06665	1.05220	1.08693	−1.49 %	−1.87 %	−3.20 %
k_l	0.85326	0.85368	0.85371	0.86723	−1.61 %	−1.56 %	−1.56 %

PMSM 15/14, $M_s = 540$, $N_p = 61$ rotor positions, piecewise-constant surface basis, $k_f = 0.325$ (inert in the mesh columns, Sect. IV.c), linear solver at $\mu_r = 3000$ throughout; unknowns 5400 at $n_{sh} = 1$, 6480 at $n_{sh} = 2$, 1260 surface columns for the lumped network. Reference values are read from the finite-element project and deviations are formed on full-precision values. k_r is computed retaining the outlying gap magnetomotive force discussed in the text; excluding it gives a second reference, 1.0664, against which the three deviations are +0.40 %, +0.02 % and −1.34 %. The deviations on the peak flux linkage, the phase self-inductance, the synchronous inductance and the fundamental gap flux density are bounds, each being smaller than the dispersion the tiling alone produces on that quantity (Table 4); the mutual inductance is the exception, the two models bracketing the reference from opposite sides. Over the seventeen quantities the two iron models are within one quantity of each other; the case for the mesh is not that it is closer but that it carries no fitted constant.

The air-gap field is shown in Fig. 4. The fundamental air-gap flux density deviated by +0.28 % on the lumped column and +0.31 % at one shoe layer, and the radial component by less than a percent in both mean and peak; the tangential component, which a radial-branch network cannot produce and which the operator supplies, deviated by +7.43 % on the lumped column and +3.22 % on the mesh. In the internal magnetic circuit the magnetomotive forces per magnet and per gap deviated by less than a percent on the lumped column; one gap value in the reference lies apart from its thirteen neighbours at 531 A, and both determinations of the reluctance factor are given without selecting between them, 1.08693 with the outlier retained and 1.0664 with it excluded. The magnetomotive forces also locate the working point of the magnet, which H2 assumes to lie on the recoil line: a drop of 762.9 A across 3.5 mm is a demagnetising field of 218 kA/m, at which the recoil line gives $B_m = B_{rem} - \mu_0\mu_r H = 0.963$ T, 77 % of the remanence, consistent with the 0.99 T peak and the 0.85 leakage factor of the table;

the reference project describes the magnet by its recoil line as well, and the on-load demagnetising field is not computed here.

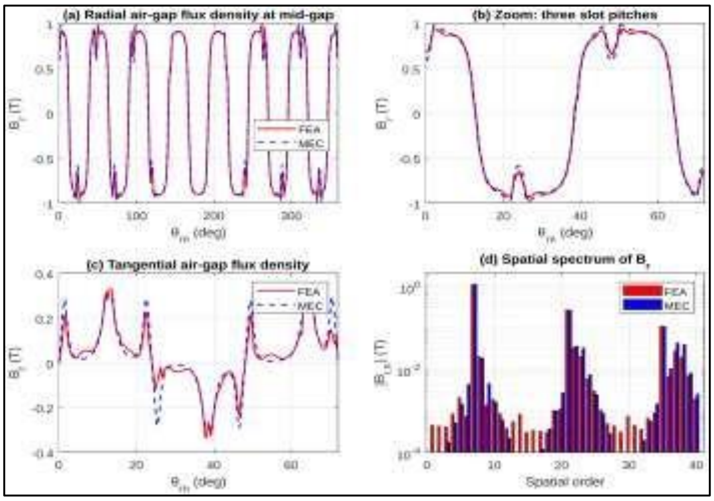

Fig. 4. Air-gap flux density of the 15/14 PMSM at no load, DtN operator versus 2-D FEA: (a) radial component at mid-gap, (b) the same over three slot pitches, (c) tangential component, (d) spatial spectrum of B_r. The tangential component, which a radial-branch network cannot produce, follows from (16) at no additional cost.

On terminal quantities the peak flux linkage deviated by +1.11 % on the lumped column and +0.24 % on the mesh, and the back-electromotive force and six-step envelope followed the same ordering (Fig. 5). The self-inductance deviated by +1.12 % and +0.34 %, the mutual by +4.09 % and −5.48 %, so the two models bracket the reference mutual from opposite sides, and the synchronous inductance by +1.24 % and +0.10 %. Registration was established once on the flux linkage, at an offset of 143.49° electrical, and held fixed; the residual optimal shift was −0.5°, and the residual root-mean-square differences were 0.0036 Wb on flux linkage and 6.7 V on electromotive force, 1.4 % and 2.9 % of the respective peaks, the only waveform-level error measures here. In the spatial spectrum of the lumped network at mid-gap, the pole harmonics deviated by at most 2.4 %, +0.3 % on the fundamental (1.0775 T against 1.0746 T), −2.4 % at $3p$ (0.2593 against 0.2657 T) and −1.9 % at $5p$ (0.1047 against 0.1067 T), while the first slot sidebands, reported as bounds because the tiling alone moves that column by 26.126 %, deviated by −8.1 % and +7.6 %, and the second pair, orders 23 and 37, by +61.1 % (0.0325 against 0.0202 T) and +57.6 % (0.0427 against 0.0271 T), governed by the tooth-tip singularity of Sect. VII.c.

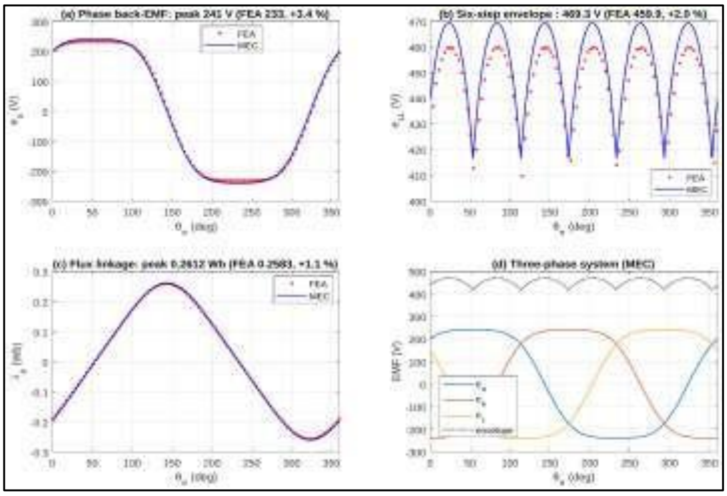

Fig. 5. Back-electromotive force and flux linkage at 1500 rpm: (a) phase back-EMF, (b) six-step envelope, (c) flux linkage, (d) the three-phase system and its envelope from the network. A single angular alignment, established on the flux linkage, the primary, non-differentiated quantity, is used for all views.

Losses. Magnet eddy-current losses follow

$$J_z = -\sigma \tilde{A}, \qquad P = \sigma L \int_S \tilde{A}^2 \, dS, \qquad \tilde{A} \equiv \frac{\partial A}{\partial t} - \left\langle \frac{\partial A}{\partial t} \right\rangle_S \tag{42}$$

in which A is the axial magnetic vector potential in the rotor frame, σ the magnet conductivity and S the magnet cross-section, the subtraction of the section mean imposing zero net current in each magnet. The two field sources give different values for the same quantity, and both are reported with the source declared: at no load the magnet eddy-current loss was 0.2036 W from the one-branch-per-tooth field and 0.2516 W from the polar mesh, against 0.334 W in the reference, that is −39.1 % and −24.7 %, on a chain frozen for this quantity at $N_p = 241$, 1688 rpm and $\sigma = 5.5556 \times 10^5$ S/m, which integrates the magnet thickness on seven equally spaced radii; the computed loss moved by 0.2 % between 181 and 481 rotor positions. The magnet eddy-current loss is declared not validated, the reference being unable to resolve it (Sect. VII.b). Equation (42) neglects the reaction of the induced currents, which is licit only while the skin depth exceeds the magnet thickness: at the dominant slotting frequency seen from the rotor, $f = N_s n/60 = 422$ Hz at the no-load test speed, the skin depth $\delta = \sqrt{\rho/(\pi f \mu_0 \mu_r)}$ is 32.25 mm against a magnet thickness of 3.5 mm, a ratio of 9.2. The no-load iron loss is 21.3358 W against 19.7298 W in the reference, +8.14 %; its eddy-current term is formed on the time derivative of the flux density, and formed instead on the Bertotti amplitude expression the same loss is 22.7409 W, +15.3 %, the two formulations differing by 6.59 %. A loss is the sum of a volumetric part, which converges under refinement, and a corner part, which does not, and the share carried by the shoe cells drifts by about twenty per cent under refinement while the total moves very little; the +8.14 % is therefore the deviation of a quantity whose convergence is not established.

Drive behaviour. The network also carries a drive chain, closure, iron model, saturable flux-linkage and torque maps $\lambda_k(\theta_r, i_\alpha, i_\beta)$ and $T(\theta_r, i_\alpha, i_\beta)$ and current loop, whose on-load transient and speed sweep at a 500 V dc bus were compared with the transient reference studies; those comparisons exercise the whole chain, so their deviations are not attributable to the air-gap operator and are given for completeness, as bars 17 to 29 of the synthesis figure below. On the on-load transient the network settled at 1257.029 rpm against 1339.826 rpm in the reference, a deviation of −6.18 %, with a phase current at that settled point of 1.41857 A against 1.55162 A, an electromagnetic torque of 4.949 N m against 4.867 N m, a copper loss of 69.43 W against 71.56 W and an iron loss of 19.08 W against 18.47 W; the two columns are therefore not read at a common operating point, and the efficiency, 86.33 % against 86.51 %, a difference of 0.2 points, is obtained at that operating point and nowhere else, the reference figure being the solver's own efficiency output, the comparison functional of Sect. V itself. The reference's own current and copper loss imply $R_{ph} = 9.908\ \Omega$, 3.1 % below the 10.2223 Ω used by the network, so the two models do not share the same winding temperature, which is the concrete reason the protocol of Sect. V asks for the phase resistance four-wire at a recorded temperature. Over the speed sweep the standstill torque deviates by +4.95 % (30.68 against 29.23 N m), the no-load speed by −1.3 % (1658 against 1680 rpm) and the peak power by −25.4 % (1115 W at 642 rpm against 1495 W at 929 rpm), while the terminal envelopes agree at a common speed, 487 V against 482 V at 1446 rpm and 477 V against 468 V at 1159 rpm. The power deficit is placed in the current and not in the electromagnetic conversion: over the twenty-eight points above 100 rpm the mean absolute deviation is 15.1 % on torque per ampere against 25.8 % on torque, 25.3 % on phase current and 38.1 % on dc-bus current, the phase current being unable to settle within the 60° interval between commutations at mid speed; at 872 rpm the network carries 5.59 A against 9.14 A in the reference, where 11.12 A would flow if the electrical transient were complete. The loss structure is reproduced, the operating point is not. The standstill torque and the magnet losses are declared not validated, the reference being unable to resolve either; on load the magnet loss is 1.578 W against 3.183 W, but the two runs differ by a factor of 0.736 before any modelling error enters, and normalised to a common operating point the deviation is −32.6 %, or −42.0 % on the copper-loss-derived currents.

Audit of the reference. Five tests and one positive confirmation bear on the reference, and none requires it to be re-solved. Test 1, the order rule: only multiples of 210, the least common multiple of 15 and 14, are physically admissible; the magnetostatic reference, 220.2 mN m peak-to-peak, peaked at order 42, where it carried 77.07 mN m, and placed 90.1 % of its spectral energy at multiples of the pole number, 1.1 % at multiples of the slot number only and 8.7 % broadband, and none at multiples of 210, where the model, 1.255 mN m peak-to-peak with 0.628 mN m at order 210, placed all of its own. Test 2, remeshed against sliding band: solved with a preserved mesh the same machine gave 0.883 mN m at order 42 against 77.04 mN m when the mesh is regenerated at each position, a factor of 87, all other settings identical; read against the noise of its own data set, the order-42 component was 40σ in the magnetostatic sequence and 2.6σ in the transient run, the latter below its own 3σ floor of 1.021 mN m. Test 3, the angular Nyquist limit: at a 1° step over the revolution the reference's Nyquist order is 180, so order 210 is not representable, whereas the model samples one pole pitch at 840 positions, 56 per cogging period, a Nyquist order of 5880. Confirmation 4a: a surrogate carrying the residual amplitude spectrum with randomised phases matched the reference to 60.56 mN m against 60.53 mN m and accounted for 100.1 % of its variance. Test 4, the energy balance: on the on-load transient it closed to 11.7 % over the run and 52.7 W in steady state, or 6.4 % of the input. Test 5, the averaging window: at the first sweep point the reported root-mean-square phase current, 24.351 A, coincided with the mean dc-bus current, 24.352 A, which a 120° conduction pattern forbids.

The admissible reference for cogging (Fig. 6) is therefore the preserved-mesh transient run, 0.604 mN m peak-to-peak with a 2σ uncertainty of 1.401 mN m at order 210, against 1.255 mN m from the model. The two dispersions quoted here are not the same statistic: 0.340 mN m is the standard error of the order-42 amplitude in the transient data set, the standard deviation of the residual, 2.42 mN m, times $\sqrt{2/N}$ over its $N = 101$ positions, while 1.401 mN m is a 2σ interval on the peak-to-peak amplitude at order 210. The outcome is a non-rejection and not a validation, since with an interval of that width any prediction below roughly 2 mN m, including zero, is compatible with the reference.

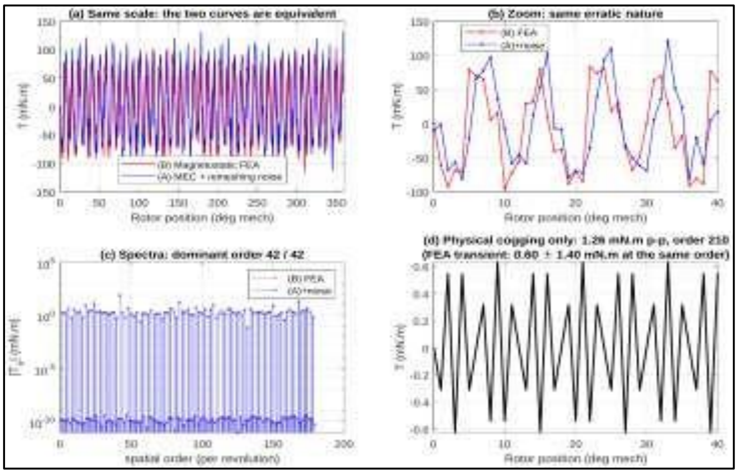

Fig. 6. Cogging torque of the PMSM: (a) the magnetostatic reference and the model with the reference's remeshing noise added, on the same scale; (b) zoom; (c) spectra, dominant order 42 in both, which the 15/14 combination cannot contain; (d) the physical cogging predicted by the model, 1.255 mN m peak-to-peak at order 210, against 0.60 ± 1.40 mN m at the same order in the transient reference. The residual of the reference is shown to be remeshing noise by a surrogate with identical amplitude spectrum, so the cogging comparison is a bracket and not an agreement.

Synthesis of the comparison set. Figure 7 collects the twenty-nine compared quantities, from the air-gap field to the speed sweep, each bar carrying its own deviation; the same values are tabulated at full precision, with their provenance, in the deposited archive. Of the twenty-eight comparable quantities, the electromotive-force constant being struck because it compares the network's no-load six-step envelope at 1500 rpm divided by the speed with the loaded terminal envelope $V_{dc} - 2Ri$ of the reference sweep, twenty fall within five per cent, the eight exceeding it being the tangential field, the on-load phase current, the no-load iron loss, the two magnet losses, the settled speed, the dc-bus current and the peak power; excluding the three declared not validated, the two magnet-loss bars and the standstill torque, the count is nineteen of twenty-five. Three quantities lie within one point of the threshold and all inside it, the mutual inductance at +4.15 %, the standstill torque at +4.95 % and the peak efficiency at −4.46 % relative, −3.99 in points. The synthesis chain forms the armature problem with an iron permeability of 5000 instead of the 3000 of Table 7 and sweeps 721 rotor positions instead of 61, which is why its inductance, electromotive-force and magnetomotive-force rows differ from the lumped column of Table 7 in the third or fourth significant figure. The field bars are bounds and not agreements, and the drive bars are read at an operating point the reference does not share.

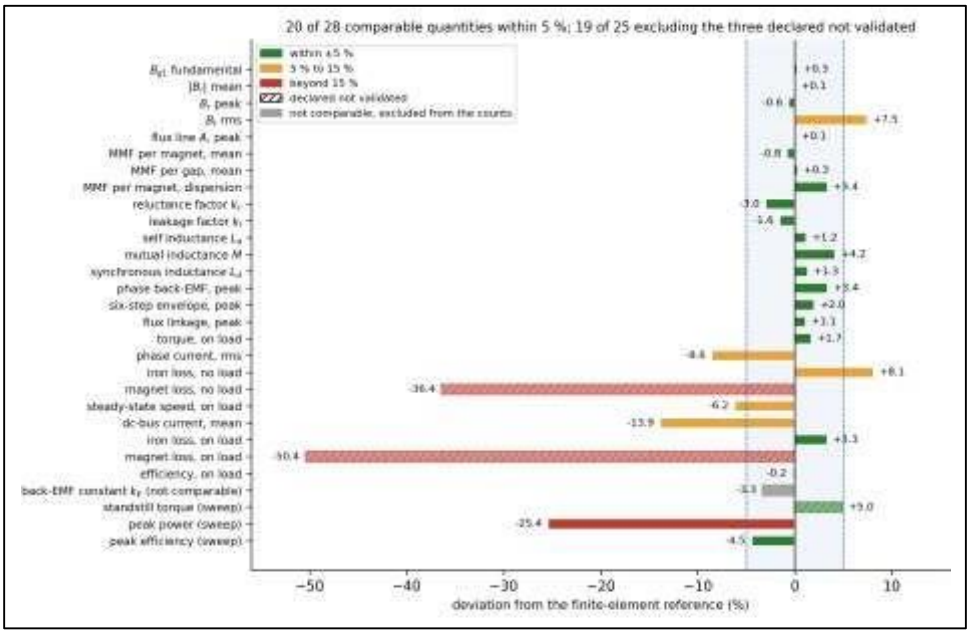

Fig. 7. Synthesis of the PMSM validation, computed on the lumped iron model, which every result of Sect.

VI uses except the two mesh columns of Table 7: deviation from the finite-element reference for the twenty-nine compared quantities, from the air-gap field to the speed sweep. Bar 26, the electromotive-force constant, compares two different quantities and is drawn grey and struck from the counts. Of the twenty-eight comparable quantities twenty fall within 5 %; excluding the three declared not validated (hatched), the count is nineteen of twenty-five.

d. Computational cost

The bore operator is assembled as (11), two products of an M_s by N array by its transpose, so the assembly costs $O(NM_s^2)$ and, under the rank condition, $O(M_s^3)$; the result is dense and symmetric and occupies $8M_s^2$ bytes in double precision, 9.33 MB at $M_s = 1080$, 12.7 MB at the 1260 surface nodes used for the position sweep and 597 MB at the finest tiling of Table 4, so that block, and not the iron, is what bounds the tiling. Its factorisation is $O(M_s^3)$ and each subsequent solve $O(M_s^2)$, and on a geometry with one smooth bounding surface the operator does not depend on rotor position, which enters only through the source vector, assembled in $O(M_sN)$: a sweep of N_{pos} positions in the linear chain costs $O(M_s^3 + N_{pos}M_s^2)$ instead of the $O(N_{pos}M_s^3)$ a position-dependent interface requires. Measured on the archived timing script at $M_s = 1260$ on the linear chain, the assembly costs 0.137 s and one dense factorisation of the reduced matrix of order 1289 costs 0.247 s; a single position then costs 0.4119 s in total and 128 positions 0.4895 s, so the marginal cost of one further position is 0.61 ms, of which the back-substitution is 0.17 ms, and 721 positions cost 0.7693 s at the solve stage. Reassembling and refactorising the operator at each position, the arithmetic a position-dependent interface imposes, costs 0.367 s per position and brings the 128-position sweep to 46.97 s, a factor of 96 on the sweep and of 600 on the margin; that factor is internal to the formulation and is not a ratio against finite elements, for which none is reported, the two solvers having been run on different hardware, to different error targets and under different stopping rules. The complete 721-position cogging call, which at every position also rebuilds the source, reconstructs both field components and forms the Maxwell stress, costs 1.965 s, or 2.73 ms per position. Over the tilings of Table 4 the total solve time scales as $M_s^{2.57}$ to $M_s^{2.60}$ and the operator assembly as $M_s^{2.61}$ to $M_s^{2.66}$, short of the cubic because the sweep is still pre-asymptotic; the archived entry point, which computes the no-load field, the circuit quantities and the cogging sweep of the lumped chain, runs in a median 18.91 s over five repetitions on a laptop with an Intel Core i5-11400H processor at 2.70 GHz and 16 GB of memory under MATLAB R2024a.

VII. Discussion

a. The operator against the closures it replaces

Agreement with finite elements is necessary but not sufficient: the formulation must also improve on the closure it replaces. Table 1 isolates that comparison, every network row using the same one-branch-per-tooth iron network at the same rotor position against the same reference, so that only the closure changes.

The Carter row is quoted in full so that it can be checked. With $b_0 = 2.000$ mm, $g' = g + h_m/\mu_r = 4.3686$ mm and a slot pitch $\tau_s = \pi D/N_s = 14.5259$ mm, the exact conformal-mapping form

$$\gamma = \frac{4}{\pi}\left[x\arctan x - \ln\sqrt{1 + x^2}\right], \qquad x = \frac{b_0}{2g'}, \qquad k_C = \frac{\tau_s}{\tau_s - \gamma g'} \tag{43}$$

gives $x = 0.22891$, $\gamma = 0.033072$ and $k_C = 1.010046$. A smooth gap with Carter's factor produces no slot sideband at all and underestimates the tangential field by 19.7 %, the residual it retains coming from the transitions between magnets rather than from slotting; and every closure of that family returns the same fundamental, 1.0958 T, because a modulation whose period is the tooth pitch creates harmonics only at orders $p \pm kN_s$ and, once normalised to unit mean, leaves order p untouched. A permeance function modulates the amplitude of a field it has not corrected.

What separates the operator from a tooth-to-tooth permeance function is not accuracy but determination. The decay of such a function is parameterised by γ_m and γ_z, which in the construction of Ostović [1] are $|a_t - a_r|/2$ and $(a_t + a_r)/2$, with a_t and a_r the arcs of the elements on the two surfaces; neither follows from the geometry of the machine. Implemented as its authors specify [17], the family reaches −8.7 % on the first sideband against −8.1 % for the operator, but over three tangential discretisations of the same machine that column ranges from −96.4 % to +170.1 %: it is undetermined, in the precise sense that the geometry does not fix its parameters and the mesh does, and the operator has no such parameter to fix.

The closest closure is the air-gap element. Condensing the same surface operator over a single layer, with the magnet meshed in the network instead of carried by the operator, is the air-gap element as that family is normally built [26], [27]; it is the N4 row of Table 1. Carrying the magnet exactly in the same code reproduces the N3 row to a relative 1.8×10^{-15} on the fundamental, so the two constructions share one operator and differ only in what is asked of the network; the same panel shows the rotor interface losing rank as soon as its column count exceeds $2N + 1$, the reciprocal condition number falling to 4.7×10^{-24} at 2520 columns for $N = 630$, the rank condition (13) recovered on a sliding interface. On this machine the difference is +4.3 % on the fundamental against +0.3 %, −13.5 % on the first sideband against −8.1 %, and +30.4 % on the tangential field against +7.4 %, and a magnet represented by radial branches is the whole of it. The second difference appears in no deviation column: because one bounding surface is smooth, the two-layer operator is invariant with rotor position and a sweep reuses a single factorisation, whereas a sliding interface is re-formed at every position; measured per position on one chain, at thirty-two positions and in two dated runs, the cost is 0.056 and 0.061 s for the position-invariant operator, 0.337 and 0.327 s when the same operator is reassembled and refactorised at every position, and 0.714 and 0.712 s for the air-gap element with its sliding interface, ratios that are lower bounds since the first chain also computes torque diagnostics at every position.

Two published closures complete the comparison, and one of them wins a column. The first-order relative permeance of Zhu and Howe [14] and the complex relative permeance of Žarko, Ban and Lipo [15] were evaluated from published implementations, the tooth ratio fixed by the real slot opening and nothing else adjusted. The complex map reproduces the first slot sideband to +0.1 % against −8.1 % for the operator, a difference inside the ±26 % tiling dispersion of that column and therefore not an ordering, but it falls to −51.0 % on $\nu = 22$ and −10.5 % on the tangential field, where the operator gives +7.6 % and +7.4 %; the first-order permeance is structurally further off, a single-harmonic modulation returning two sidebands of equal amplitude, 85 and 91 per cent low, and no slotting tangential field at all. Both modulate a slotless solution obtained with infinitely permeable iron, and neither carries a saturable iron model or couples to a network as a condensation. The subdomain family is not represented, its implementation here idealising the semi-closed slot as an open one and drifting by forty per cent on the sidebands over its admissible truncation.

b. What the reference can and cannot resolve

The cogging outcome of Sect. VI.c is a bracket and not an agreement, and the audit explains why: the magnetostatic reference is not a measurement of cogging torque but of cogging torque plus remeshing noise, and the surrogate accounts for its variance entirely, leaving nothing for a model to predict. The five tests generalise beyond this machine, since none requires the reference to be re-solved, which is the common situation when a reduced-order model is validated against results supplied by a third party.

One limit belongs to the extraction and not to the solution. Read from the same magnetostatic study, the fundamental gap flux density is 1.074551 T when the bore profile is interpolated onto a uniform 3600-point grid and 1.074918 T when it is taken on the solver's own 1001-point output, a spread of 0.034 %; on the first slot sideband the same two conventions give 0.019658 T and 0.018664 T, a spread of 5.3 %, and on $\nu = 22$, 0.031794 T against 0.032760 T, a spread of 3.0 %. Both are formed from the same exported profile of 1001 points spanning 0 to 359.906414°, and it is the missing 0.0936°, 0.026 % of the turn, that separates them: the second convention takes the amplitude on points that are not a whole number of periods of the slot harmonics, the leakage growing with the order, −0.03 % at order 7, +5.3 % at 8, +0.30 % at 21, +3.0 % at 22 and +5.1 % at 23. Every deviation quoted in this paper uses the first convention; on the fundamental the extraction spread is thirteen times smaller than the tiling floor, while on the slot sidebands it is of the size of the deviations themselves, a second and independent reason to report those as bounds.

The uncertainty budget produces no band on B_{g1}, on L_d or on any other field quantity, and none is asserted anywhere in this paper. A deviation of a few tenths of a percent on a field quantity cannot be attributed to the model rather than to the discretisation of the reference, because the size of the second is unknown, the tooth-tip singularity is present in the reference mesh too, and the transient studies carry the mesh written into the project, with length constraints of 10 mm on the iron and 1.75 mm on the magnets, rather than one selected by a convergence criterion. The comparison carries its full weight only where the deviation is large enough to survive any plausible band, as it is on the lumped column and on the mutual inductance, and as it is not on the 0.10 % of L_d or the 0.24 % of the flux linkage: the tiling alone moves the peak flux linkage by 0.612 % and the synchronous inductance by 1.777 % (Table 4), so the three headline figures are bounds, 0.31 % against a 0.440 % floor, 0.24 % against 0.612 %, 0.10 % against 1.777 %, the mutual inductance being the exception, its deviation exceeding the 2.039 % the tiling produces on it in both columns.

c. Bounds of validity: why the method works, where it fails

Why the method works. The annulus is the one region of the machine in which the field equation is linear and separable, so its exact solution is a Fourier multiplier, and a multiplier condensed by Galerkin projection onto the bore nodes enters the nodal system as one more branch block. The iron, where the nonlinearity lives, is left to the network, which is what a reluctance network does well, and the magnet enters the same multiplier as a source, so the two-media annulus costs nothing more than a bare gap. The agreement of Sect. VI.c on the fundamental, the flux linkage and the inductances follows from three facts that Levels 1 and 2 establish separately: the operator is exact, its condensation on the machine is locked to a stationary bracket, and the coupled system is symmetric positive definite and solved to a residual of 10^{-9}.

Under which conditions. The construction rests on the five hypotheses of Sect. II.a, of which two bound its use. The bore must be a circle for the symbol to be diagonal in the Fourier basis: a stator with a non-circular bore, or a rotor with surface features, breaks H2 and requires either a second slotted surface, which loses position invariance, or a matched subdomain. The magnet must sit on its recoil line: a working point that leaves it, under demagnetising armature reaction, makes the magnet layer nonlinear and removes the exactness of the surface map. The conformity condition is one of order and holds for every operator of order one or higher; it does not depend on the geometry.

Where it fails, and why. Two quantities do not converge with mesh refinement, the first slot sideband and the synchronous inductance, and for the sideband the two refinement directions disagree (Sect. VI.b). There is a singularity, and the network does not introduce it: the tooth tip is a sharp corner in the reference model itself, the fillet being applied inside a boolean block, and the re-entrant corner carries an $r^{\lambda-1}$ field with $\lambda < 1$ [49], [50], so the computed value depends on the cell size at the corner in the network as in the finite-element mesh. Saturating the corners lowers their permeability, deepens the permeance dip under the slot opening and strengthens the slot modulation, which a linear model cannot produce and therefore underestimates, while Newton produces it and overshoots. On the first slot sideband the lumped network is the closest of the three models to the reference, −8.12 % against −13.34 % and −19.58 % for the refined mesh (Table 7), all three lying inside the ±26 % the tiling alone moves this column; the quantity is singular, its value is set by the cell size at the corner, and a model with one cell there has no more claim to the right answer than a model with eight, so reporting that proximity as a result about the model would be reporting an accident. That defect and the harmonic tail of Sect. III are the same failure of regularity seen in two bases, one repairable by changing the trial space and the other present in the reference as much as in the network. The criterion for a new machine is twofold: form the logarithmic thickness of the air layer to locate the tail, and check whether the truncation is free of the tiling.

Losses, cost and gain. Losses are excluded from the integral-quantity rule, because their total can look stable while their corner share drifts, as the no-load iron loss of Sect. VI.c shows, and the magnet eddy-current loss is declared not validated because the reference cannot resolve it. The condensation replaces the annulus and the magnet, which would otherwise be meshed, by a dense $M_s \times M_s$ block: on the linear chain that block is assembled and factorised once per machine and every rotor position costs one back-substitution and one source assembly, 0.61 ms at $M_s = 1260$ against 367 ms for a reassembled and refactorised interface, and that gain holds whenever one bounding surface is smooth. The cost is the density of the block, $8M_s^2$ bytes, which bounds the tiling at a few thousand columns on a laptop, and, on the nonlinear chain, the refactorisation of that block inside every Newton iteration, since the half-branches touching the bore are iron; the three fitted constants of the lumped counterpart disappear with the mesh, whose price is 5400 to 6480 unknowns against the thirty interior unknowns of the lumped chain.

What is general and what belongs to this geometry. Proposition 1, Corollary 1, Propositions 2 and 2′ and the diagnostic hold for any surface operator whose symbol is bounded above and below by multiples of n^α, $\alpha \geq 1$, condensed onto a contiguous tiling, and Proposition 3 for any such operator of order one under the rank lock; the constant $c = \mu_0 L/\pi$ and the bracket depend on the active length and the column width only, and the limits of Proposition 3 and of (32) on nothing at all. The size of the exact-kernel correction, the order at which the tail installs itself and the position invariance are properties of this annulus: a bare gap ten times thinner would raise the correction to a tenth of the diagonal at $N = 10^7$ and push the tail to order 330, and a second slotted surface would remove the invariance. The floors of Table 4, the corner-governed brackets and every deviation of Sect. VI.c belong to the 750 W machine and to its reference, and none is carried to another machine without the protocol of Sect. V being run again. Four rules follow: integral quantities are reported as bounds on this machine and not as validated outputs, the word validation being reserved for a deviation resolvable above the tiling floor; the first slot sideband, the cogging torque and any quantity built from them are bounds and must carry the solver and the corner discretisation used; losses are excluded from the integral-quantity rule; and the method is not suitable, on the present evidence, for acoustic-noise prediction or for cogging-torque design.

VIII. Conclusion

The air-gap region of a magnetic equivalent circuit was closed by the exact Dirichlet-to-Neumann operator of a two-layer annulus, the magnetisation carried as a source inside the same surface map, and condensed onto the surface nodes of a saturable reluctance network solved by Newton on the differential reluctance. The central result concerns that condensation rather than the operator. Under a piecewise-constant bore basis, which is what a reluctance network in nodal form imposes, the self-energy of a column grows as $(2\mu_0 L/\pi)\ln N$ without bound and its two nearest-neighbour entries fall as $-(\mu_0 L/\pi)\ln N$: the condensed operator has no limit as the truncation grows at fixed tiling, and when the truncation is locked to the tiling by the rank condition it converges instead to a definite operator that is neither the continuous one nor the one the closed forms describe (Proposition 3), so that the truncation selects a value rather than approximating one. A continuous piecewise-linear basis restores an absolutely convergent series with a residual tail in $1/N^2$, is a conforming Galerkin method with a proved approximation estimate that survives the locking, and costs one line of code; carried through the validated chain it reproduces the compared quantities to within the dispersion the tiling alone produces, so the repair costs nothing where the truncation is locked, and once the truncation is released only the conforming basis holds. What is established is the conformity of the surface condensation and the estimates (34)–(36) on the model problem of the condensation alone; what is not claimed is any convergence theory for the composite method, since no continuous problem exists of which a reluctance network is a consistent approximation. The result applies wherever a surface operator of order at least one is condensed onto a discontinuous basis, and the diagnostic that reveals it, the ratio of successive increments, is available to anyone who can run the same sum twice, its limit being one for a logarithmic tail and $2^{\alpha-1}$ for a symbol of order α.

For the electrical engineer the consequences are three. Against two-dimensional finite elements on a 750 W, 15-slot/14-pole machine, with every configuration declared per table, the mesh model, which carries no fitted constant, deviates by 0.10 % on synchronous inductance, 0.24 % on flux linkage and 0.31 % on the fundamental air-gap flux density, and the lumped model, which carries three fitted constants, by 1.24 %, 1.11 % and 0.28 %. All three are bounds and not agreements, each being smaller than the dispersion the locked tiling alone produces on its own quantity, 1.777 %, 0.612 % and 0.440 % (Table 4); a comparison is called a validation here only when its deviation is resolvable above that floor and the quantity carries no fitted constant. The synchronous inductance does not converge over the refinement sequence examined, so the figure quoted is the value of a declared configuration and not of a limit, and refining the shoe moves thirteen of the seventeen tabulated quantities away from the reference rather than towards it; the case for the mesh is not that it is closer but that it carries no fitted constant. Second, the operator returns the tangential field and with it a Maxwell-stress torque that a radial-branch network cannot form, and the closures it replaces are either undetermined by the geometry, as the tooth-to-tooth family is, or blind to the slot harmonics, as Carter's factor is. Third, because the operator is invariant with rotor position whenever one bounding surface is smooth, a rotor sweep costs one factorisation and one back-substitution per position, 0.61 ms against 367 ms per position on the archived chain.

The paper also delimits what the method does not do. The first slot sideband and the cogging torque are governed by a tooth-tip corner singularity, are bracketed by the two solvers, and the bracket does not close under refinement; the magnet losses and the standstill torque are declared not validated, the reference being unable to resolve either; and the drive-chain comparison reproduces the loss structure but not the operating point. No experimental comparison is made anywhere in this paper: every deviation reported here is between two numerical models. The five-test procedure proposed for auditing a finite-element reference without re-solving it is independent of the formulation and reusable on its own; a reduced-order model cannot stand closer to the machine than the reference against which it is measured, and that reference is not always what it appears to be.

Three items follow in order of priority: a corner treatment for the tooth tip, a graded mesh, a singular enrichment or a fillet resolved on both sides, without which the slot sidebands remain bounds in the network and in the reference alike; a controlled timing comparison of the two methods on identical hardware and to a common error target, together with the two open-circuit measurements of Sect. V on a prototype; and the extension of the conformity result to a tiling of unequal columns, on which an asymmetric hat whose half-widths are the local half-steps of the grid restores the partition of unity and keeps the projection in closed form.

Data availability. The MATLAB chain for the machine validated here, the dated execution transcripts from which every published value is read, the manifest binding each published quantity to the chain that produced it, the finite-element exports used as the reference, the diagnostic scripts of Sects. VII.b and VII.c, the uncertainty budget and the full table of the twenty-nine compared quantities are available in the repository https://github.com/il1996/mec-dtn-airgap-PMSM at the tagged release v1.2.0, which also carries an independent recomputation, from the equations of Sect. III alone, of the closed forms of Proposition 1 and of the panels of Tables 3 and 4. The code is released under the MIT licence and the data and documents under CC BY 4.0, except the finite-element exports, whose redistribution is subject to the solver licence as stated in the archive.

Declarations. Funding: no funds, grants or other support were received during the preparation of this manuscript. Competing interests: the authors have no competing interests to declare. Author contributions: conceptualisation, I.L.; methodology, I.L. and A.B.; software, formal analysis, investigation and visualisation, I.L.; validation, I.L., A.B., N.M. and S.L.; writing, original draft, I.L.; writing, review and editing, A.B., N.M. and S.L.; supervision, A.B., N.M. and S.L. All authors read and approved the final manuscript.

References

[1] V. Ostović, *Dynamics of Saturated Electric Machines*. New York, NY, USA: Springer, 1989.

[2] S. D. Sudhoff, B. T. Kuhn, K. A. Corzine, and B. T. Branecky, "Magnetic equivalent circuit modeling of induction motors," *IEEE Transactions on Energy Conversion*, vol. 22, no. 2, pp. 259–270, 2007.

[3] M. Amrhein and P. T. Krein, "3-D magnetic equivalent circuit framework for modeling electromechanical devices," *IEEE Transactions on Energy Conversion*, vol. 24, no. 2, pp. 397–405, 2009.

[4] V. Ostović, "A method for evaluation of transient and steady state performance in saturated squirrel cage induction machines," *IEEE Transactions on Energy Conversion*, vol. EC-1, no. 3, pp. 190–197, 1986.

[5] S. R. Hosseini, M. Abedini, and M. Davarpanah, "A straightforward condition monitoring algorithm for static air gap eccentricity detection in SCIM using the magnetic equivalent circuit model," *Electric Power Systems Research*, vol. 253, p. 112552, 2026.

[6] M. F. Hsieh and Y. C. Hsu, "A generalized magnetic circuit modeling approach for design of surface permanent-magnet machines," *IEEE Transactions on Industrial Electronics*, vol. 59, no. 2, pp. 779–792, 2012.

[7] T. Sapmaz and Y. Oner, "Improved magnetic equivalent circuit for dual stator consequent pole permanent magnet machine," *Journal of Magnetism and Magnetic Materials*, vol. 550, p. 169039, 2022.

[8] L. Zhang, "An efficient modeling of air gap and nonlinear analysis of magnetic equivalent circuit for large turbogenerators under no-load condition," *IEEE Transactions on Magnetics*, vol. 58, no. 2, pp. 1–8, 2022.

[9] G. Watthewaduge and B. Bilgin, "Sizing of the motor geometry for an electric aircraft propulsion switched reluctance machine using a reluctance mesh-based magnetic equivalent circuit," *Machines*, vol. 11, no. 1, p. 59, 2023.
[10] M. Heidary, P. Naderi, and A. Shiri, "Modeling and analysis of a multi-segmented linear permanent-magnet synchronous machine using a parametric magnetic equivalent circuit," *Electr. Eng.*, vol. 104, no. 2, pp. 705–715, 2022.
[11] C. Liu, Z. Chao, S. Wang, and Y. Wang, "A quick electromagnetic performance analysis method for permanent magnet claw pole machine based on combined analytical and equivalent magnetic circuit method," *Electr. Eng.*, vol. 105, no. 3, pp. 1541–1553, 2023.
[12] F. W. Carter, "The magnetic field of the dynamo-electric machine," *Journal of the Institution of Electrical Engineers*, vol. 64, no. 359, pp. 1115–1138, 1926.
[13] J. Pyrhönen, T. Jokinen, and V. Hrabovcová, *Design of Rotating Electrical Machines*, 2nd ed. Chichester, U.K.: Wiley, 2014.
[14] Z. Q. Zhu and D. Howe, "Instantaneous magnetic field distribution in brushless permanent magnet DC motors. III. Effect of stator slotting," *IEEE Transactions on Magnetics*, vol. 29, no. 1, pp. 143–151, 1993.
[15] D. Žarko, D. Ban, and T. A. Lipo, "Analytical calculation of magnetic field distribution in the slotted air gap of a surface permanent-magnet motor using complex relative air-gap permeance," *IEEE Transactions on Magnetics*, vol. 42, no. 7, pp. 1828–1837, 2006.
[16] D. Žarko, D. Ban, and T. A. Lipo, "Analytical solution for cogging torque in surface permanent-magnet motors using conformal mapping," *IEEE Transactions on Magnetics*, vol. 44, no. 1, pp. 52–65, 2008.
[17] A. M. Silva, C. H. Antunes, A. M. S. Mendes, and F. J. T. E. Ferreira, "Generalized reluctance network framework for fast electromagnetic analysis of radial-flux machines," *IEEE Transactions on Energy Conversion*, vol. 38, no. 1, pp. 310–320, 2023.
[18] M. Ghods, H. Gorginpour, M. A. Bazrafshan, and M. S. Toulabi, "Equivalent magnetic network modeling of dual-winding outer-rotor Vernier permanent magnet machine considering pentagonal meshing in the air-gap," *IEEE Transactions on Industrial Electronics*, vol. 69, no. 12, pp. 12587–12599, 2022.
[19] T. Lubin, S. Mezani, and A. Rezzoug, "Exact analytical method for magnetic field computation in the air gap of cylindrical electrical machines considering slotting effects," *IEEE Transactions on Magnetics*, vol. 46, no. 4, pp. 1092–1099, 2010.
[20] F. Dubas and C. Espanet, "Analytical solution of the magnetic field in permanent-magnet motors taking into account slotting effect: No-load vector potential and flux density calculation," *IEEE Transactions on Magnetics*, vol. 45, no. 5, pp. 2097–2109, 2009.
[21] B. L. J. Gysen, K. J. Meessen, J. J. H. Paulides, and E. A. Lomonova, "General formulation of the electromagnetic field distribution in machines and devices using Fourier analysis," *IEEE Transactions on Magnetics*, vol. 46, no. 1, pp. 39–52, 2010.
[22] K. Boughrara, R. Ibtiouen, D. Žarko, O. Touhami, and A. Rezzoug, "Magnetic field analysis of external rotor permanent-magnet synchronous motors using conformal mapping," *IEEE Transactions on Magnetics*, vol. 46, no. 9, pp. 3684–3693, 2010.
[23] Z. Li, X. Huang, Z. Chen, L. Wu, Y. Shen, and T. Shi, "Electromagnetic analysis for interior permanent-magnet machine using hybrid subdomain model," *IEEE Transactions on Energy Conversion*, vol. 37, no. 2, pp. 1223–1232, 2022.
[24] W. Liu, H. Yang, H. Lin, and L. Qin, "Hybrid analytical modeling of air-gap magnetic field in asymmetric-stator-pole flux reversal permanent magnet machine considering slotting effect," *IEEE Transactions on Industrial Electronics*, vol. 69, no. 2, pp. 1739–1749, 2022.
[25] C. Zhao, M. Cheng, J. Zhou, and Z. Ma, "A linear hybrid model for analytical magnetic field analysis in flux-switching permanent-magnet machine," *IEEE Transactions on Energy Conversion*, vol. 38, no. 2, pp. 1433–1441, 2023.
[26] A. Abdel-Razek, J. L. Coulomb, M. Feliachi, and J. C. Sabonnadière, "The calculation of electromagnetic torque in saturated electric machines within combined numerical and analytical solutions of the field equations," *IEEE Transactions on Magnetics*, vol. 17, no. 6, pp. 3250–3252, 1981.
[27] A. Abdel-Razek, J. L. Coulomb, M. Feliachi, and J. C. Sabonnadière, "Conception of an air-gap element for the dynamic analysis of the electromagnetic field in electric machines," *IEEE Transactions on Magnetics*, vol. 18, no. 2, pp. 655–659, 1982.
[28] S. J. Salon, *Finite Element Analysis of Electrical Machines*. Boston, MA, USA: Kluwer, 1995.
[29] H. De Gersem and T. Weiland, "Harmonic weighting functions at the sliding interface of a finite-element machine model incorporating angular displacement," *IEEE Transactions on Magnetics*, vol. 40, no. 2, pp. 545–548, 2004.
[30] E. Lange, F. Henrotte, and K. Hameyer, "A variational formulation for nonconforming sliding interfaces in finite element analysis of electric machines," *IEEE Transactions on Magnetics*, vol. 46, no. 8, pp. 2755–2758, 2010.

[31] A. Buffa, Y. Maday, and F. Rapetti, "A sliding mesh-mortar method for a two dimensional eddy currents model of electric engines," *ESAIM: Mathematical Modelling and Numerical Analysis*, vol. 35, no. 2, pp. 191–228, 2001.
[32] Z. Bontinck, J. Corno, S. Schöps, and H. De Gersem, "Isogeometric analysis and harmonic stator–rotor coupling for simulating electric machines," *Computer Methods in Applied Mechanics and Engineering*, vol. 334, pp. 40–55, 2018.
[33] H. Egger, M. Harutyunyan, M. Merkel, and S. Schöps, "On the stability of harmonic coupling methods with application to electric machines," in *Scientific Computing in Electrical Engineering (SCEE 2020)*, Mathematics in Industry, vol. 36, M. van Beurden, N. Budko, and W. Schilders, Eds. Cham, Switzerland: Springer, 2021, pp. 117–125.
[34] S. Ouagued, Y. Amara, and G. Barakat, "Comparison of hybrid analytical modelling and reluctance network modelling for pre-design purposes," *Mathematics and Computers in Simulation*, vol. 130, pp. 3–21, 2016.
[35] I. Belmahi, S. Asfirane, G. Barakat, F. Chabour, and Y. Amara, "Axial-field switched-reluctance machine for in-wheel motor applications: Hybrid analytical modeling (reluctance network and formal analytical solution) and inductance measurements," *IEEE Transactions on Magnetics*, early access, 2026.
[36] A. Quarteroni and A. Valli, *Domain Decomposition Methods for Partial Differential Equations*. Oxford, U.K.: Oxford University Press, 1999.
[37] J. B. Keller and D. Givoli, "Exact non-reflecting boundary conditions," *Journal of Computational Physics*, vol. 82, no. 1, pp. 172–192, 1989.
[38] D. Yu and L. Zhao, "Natural boundary integral method and related numerical methods," *Engineering Analysis with Boundary Elements*, vol. 28, no. 8, pp. 937–944, 2004.
[39] Y. Xu, G. Zhang, B. Zhou, H. Wang, and Q. Tang, "Analysis of acoustic radiation problems using the cell-based smoothed radial point interpolation method with Dirichlet-to-Neumann boundary condition," *Engineering Analysis with Boundary Elements*, vol. 108, pp. 447–458, 2019.
[40] H. Ma, A. Tian, G. Sui, Q. Li, and Y. Zhang, "Analysis of acoustic radiation problems involving arbitrary immersed media interfaces by the extended finite element method with Dirichlet to Neumann boundary condition," *Engineering Analysis with Boundary Elements*, vol. 168, p. 105936, 2024.
[41] H. W. Derbas, J. M. Williams, A. C. Koenig, and S. D. Pekarek, "A comparison of nodal- and mesh-based magnetic equivalent circuit models," *IEEE Transactions on Energy Conversion*, vol. 24, no. 2, pp. 388–396, 2009.
[42] W. McLean, *Strongly Elliptic Systems and Boundary Integral Equations*. Cambridge, U.K.: Cambridge University Press, 2000.
[43] O. Steinbach, *Numerical Approximation Methods for Elliptic Boundary Value Problems: Finite and Boundary Elements*. New York, NY, USA: Springer, 2008.
[44] S. A. Sauter and C. Schwab, *Boundary Element Methods*, Springer Series in Computational Mathematics, vol. 39. Berlin, Germany: Springer, 2011.
[45] M. Costabel, "Boundary integral operators on Lipschitz domains: Elementary results," *SIAM Journal on Mathematical Analysis*, vol. 19, no. 3, pp. 613–626, 1988.
[46] J. C. Nédélec, "Integral equations with non integrable kernels," *Integral Equations and Operator Theory*, vol. 5, no. 1, pp. 562–572, 1982.
[47] M. Healey and N. Heuer, "Mortar boundary elements," *SIAM Journal on Numerical Analysis*, vol. 48, no. 4, pp. 1395–1418, 2010.
[48] F. Chouly and N. Heuer, "A Nitsche-based domain decomposition method for hypersingular integral equations," *Numerische Mathematik*, vol. 121, no. 4, pp. 705–729, 2012.
[49] P. Grisvard, *Elliptic Problems in Nonsmooth Domains*, Classics in Applied Mathematics, vol. 69. Philadelphia, PA, USA: SIAM, 2011 (reprint of the 1985 Pitman edition).
[50] J. Meixner, "The behavior of electromagnetic fields at edges," *IEEE Transactions on Antennas and Propagation*, vol. 20, no. 4, pp. 442–446, 1972.
[51] Z. Q. Zhu and D. Howe, "Influence of design parameters on cogging torque in permanent magnet machines," *IEEE Transactions on Energy Conversion*, vol. 15, no. 4, pp. 407–412, 2000.
[52] Z. Q. Zhu, D. Howe, E. Bolte, and B. Ackermann, "Instantaneous magnetic field distribution in brushless permanent magnet DC motors. I. Open-circuit field," *IEEE Transactions on Magnetics*, vol. 29, no. 1, pp. 124–135, 1993.
[53] Z. Q. Zhu and D. Howe, "Instantaneous magnetic field distribution in brushless permanent magnet DC motors. II. Armature-reaction field," *IEEE Transactions on Magnetics*, vol. 29, no. 1, pp. 136–142, 1993.
[54] P. G. Ciarlet, *The Finite Element Method for Elliptic Problems*, Classics in Applied Mathematics, vol. 40. Philadelphia, PA, USA: SIAM, 2002 (reprint of the 1978 North-Holland edition).
[55] C. Canuto, M. Y. Hussaini, A. Quarteroni, and T. A. Zang, *Spectral Methods: Fundamentals in Single Domains*. Berlin, Germany: Springer, 2006.
[56] J. Saranen and G. Vainikko, *Periodic Integral and Pseudodifferential Equations with Numerical Approximation*, Springer Monographs in Mathematics. Berlin, Germany: Springer, 2002.

[57] F. W. J. Olver, D. W. Lozier, R. F. Boisvert, and C. W. Clark, Eds., *NIST Handbook of Mathematical Functions*. New York, NY, USA: Cambridge University Press, 2010.
[58] G. Bertotti, "General properties of power losses in soft ferromagnetic materials," *IEEE Transactions on Magnetics*, vol. 24, no. 1, pp. 621–630, 1988.